Characterization of Magnetic Thin Films for Actuating Origami Devices

2018 CNF REU Intern: Sierra Russell

2018 CNF REU Intern Affiliation: Nanoscale Engineering and Applied Mathematics, SUNY Polytechnic Institute – Colleges of Nanoscale Science and Engineering

CNF Project: 2018 Cornell NanoScale Science and Technology Facility Research Experience for Undergraduates Program

CNF REU Principal Investigator: Professor Paul McEuen, Department of Physics, Cornell University

CNF REU Mentor: Tanner Pearson, School of Applied and Engineering Physics, Cornell University

Primary Source of CNF REU Funding: National Science Foundation via the National Nanotechnology Coordinated Infrastructure (NNCI) Grant No. ECCS-1542081

Contact: srussell@sunypoly.edu, plm23@cornell.edu, tgp34@cornell.edu

Website: http://www.cnf.cornell.edu/cnf_2018reu.html

Primary CNF Tools Used: Even-odd hour electron-beam evaporator, FlexUs film stress measurement system, P7 profilometer, ABM contact aligner, Class II resist room

Abstract:

Fabrication inspired by origami offers a novel method for the development of micron-scale machines, which have a wide range of potential applications. The use of magnetic thin films in tandem with ultra-thin atomic layer deposition (ALD) films allows for the creation of actuatable devices that can be controlled with external magnetic torques. We characterized cobalt, nickel, and iron films to compare their viability for these devices. We deposited our films via electron-beam evaporation at thicknesses of 25 nm and 50 nm and deposition rates of 0.3 Å/s and 0.6 Å/s, on top of a 10 nm thick titanium adhesion layer. We performed stress measurements of each film pre-and post-deposition, as well as thickness verification. We obtained the hysteresis curve of each film by using a vibrating sample magnetometer (VSM). We see that Fe and Co have significantly higher magnetizations than Ni, whereas Ni benefits from having the lowest stress. We also showed that the addition of a low stress polymer (SU-8) spun on top of the magnetic films may help to reduce the stress in the composite film. We discuss the implications of these results for our origami-inspired devices.

Summary of Research:

The goal of this work was to determine the viability of different magnetic materials for the fabrication of actuatable micron-scale devices. These devices, composed of a flexible ALD backbone and rigid magnetic panels, can be controlled with external magnetic torques to create three dimensional structures from planar Si-based processing (Figure 1). We measured the stress experienced in the magnetic films, as it imparts curvature on the underlying ultrathin ALD films and alters their bending energies. We also studied the magnetic properties of the magnetic films. These include the magnetization saturation, which relates to the magnitude of the magnetic torques we can apply, and the coercive field, which is the field required to orient the magnetic moment of the film along a given axis.

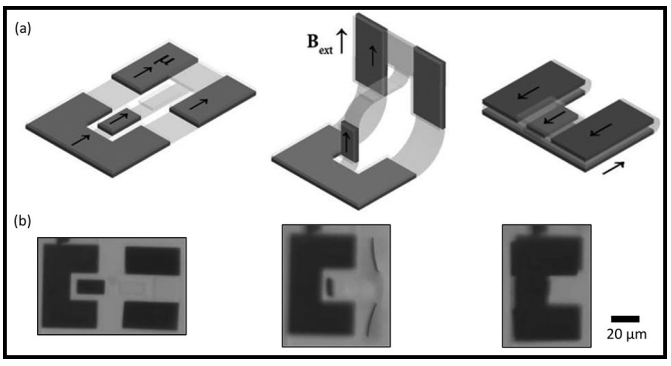

Figure 1: (a) Schematic and (b) optical image of 2D-to-3D magnetically actuated device with latching mechanism. μ represents the magnetic moment and B_{ext} the external magnetic field.

We characterized three magnetic materials: cobalt, nickel, and iron. The materials were deposited via electron-beam evaporation. A 10 nm thick titanium layer was deposited prior to any magnetic films to promote adhesion to the wafer. Each material was deposited at 25 nm and 50 nm with deposition rates of 0.3 Å/s. Additionally, we deposited 50 nm of Co at a deposition rate of 0.6 Å/s to determine the effect on the stress. Once the films were deposited, the thickness was verified using a profilometer.

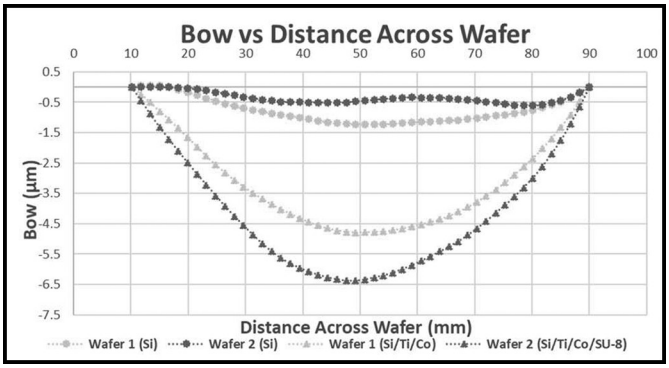

Figure 2: Bow of two wafers before and after deposition to compare the change in stress with the addition of SU-8 photoresist.

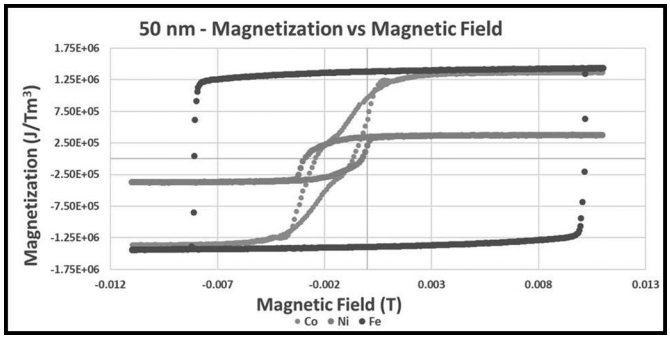

Figure 3: Magnetic hysteresis curves of 50 nm thick Co, Fe, and Ni.

Stress measurements were taken with the FlexUs film stress measurement tool. This tool measures the bow of the wafer before and after deposition. Then it relates the change in the bow with the properties of the deposited material to determine the stress in the film. To see the influence a low stress polymer has on the overall stress in a film, 70 nm of Co was deposited on two wafers in parallel, followed by spinning 1 μm of SU-8 photoresist on one wafer (Figure 2).

Samples from each thickness of each material were put through a VSM to determine their saturated magnetizations and coercivities. The data produced by the tool provides the magnetic moment as a function of the magnetic field. We normalized the magnetic moments by the volumes of the respective films to determine their magnetizations.

Results and Conclusions:

We found that Fe films have the largest amount of stress, with both the 25 nm and 50 nm thick samples having an average stress of 820 +/-14.9 MPa. The Co films had an average stress of 400 +/-19.9 MPa, and the Ni films had an average stress of 170 +/-12.0 MPa. In the case of Co, increasing the deposition rate from 0.3 Å/s to 0.6 Å/s didn't impact the stress in the film. Moreover, the addition of the SU-8 on top of the Co film did reduce the stress in the total film by approximately 90%.

The VSM data showed that Fe has the largest coercive field and magnetization saturation, while Co has the lowest coercive field and Ni has the lowest magnetization saturation (Figure 3).

The 25 nm and 50 nm samples showed similar magnetization saturations, but the coercive fields tended to increase with increasing thickness. However, we didn't expect to see Ni having a larger coercive field than Co, since Ni is considered a softer magnetic material. We think this could be due to possibly depositing oxide during our Co deposition, instead of pure Co.

We've shown that Co and Fe films have much greater stresses than Ni films, which makes them more of a risk to use as they're more likely to impact the stiffness of the ALD films in our devices. Ni films are much weaker magnets than Co and Fe films; therefore, we wouldn't be able to apply as strong of magnetic torques. To balance these factors, we can use SU-8 to reduce the stress in Co and Fe, resulting in films with both low stress and high magnetization that maximize device performance. The next steps for this project are to investigate more magnetic materials, such as magnetic alloys, and different methods of deposition.

Acknowledgements:

Thank you to Professor Paul McEuen for taking me on as an intern for this program, and Tanner Pearson for the excellent mentorship throughout the summer. This work was was performed in part at the Cornell NanoScale Science & Technology Facility (CNF) and funded by the National Science Foundation via the National Nanotechnology Coordinated Infrastructure (NNCI) Grant No. ECCS-1542081.

Development of a MEMS Tool to Study the Physics of Water and Ice

2018 CNF REU Intern: Kody Whisnant

2018 CNF REU Intern Affiliation: Chemical Engineering, Wayne State University

CNF Project: 2018 Cornell NanoScale Science and Technology Facility Research Experience for Undergraduates Program

CNF REU Principal Investigator: Dr. Abraham Stroock, Smith School of Chemical and Biomolecular Engineering, Cornell

CNF REU Mentor: Hanwen Lu, Sibley School of Mechanical and Aerospace Engineering, Cornell University

Primary Source of CNF REU Funding: National Science Foundation via the National Nanotechnology Coordinated Infrastructure (NNCI) Grant No. ECCS-1542081

Contact: kody.whisnant@wayne.edu, abe.stroock@cornell.edu, hl943@cornell.edu

Website: http://www.cnf.cornell.edu/cnf_2018reu.html

Primary CNF Tools Used: ABM contact aligner, Anatech resist strip, FilMetrics film measurement system, LPCVD nitride furnace, Oxford 81/82 etchers, Oxford PECVD, SÜSS SB8e substrate bonder, SÜSS MA6-BA6 contact aligner, VersaLaser cutting/engraving tool

Abstract:

Freezing of water in confinement is commonly found in geological, biological and architectural contexts. It is believed that the phase equilibrium and crystal formation is influenced by the confinement in pore space, which often has nanoscopic dimensions. The small scale and structural complexity of porous materials hinders our ability to understand the detail kinetics and phase equilibrium of crystals in confinement. To shed light into this problem, we developed a microelectromechanical systems (MEMS) based porous system consisting of geometrically well-defined high aspect ratio nanochannels with nanoscale (30 nm to 100 nm) channel heights and micron-scale channel width. Such configurations provide a wide field of view (~microns) for direct visualization of crystallization kinetics and phase equilibrium within nanoconfinement. Channels were first fabricated via conventional photolithography techniques on silicon and glass substrates. Notably, a 200 nm silicon nitride layer was deposited via low pressure chemical vapor deposition (LPCVD) underneath the channels to enhance contrast between liquid water and ice. The final channel geometries were verified via capillary condensation within the channels. Finally, we experimentally observed the ice-water interface in nanoconfinement. The melting of confined ice is in quantitative agreement with the Gibb-Thomson relation.

Project Summary:

Introduction. Freezing of water in nanoconfinement is of great importance in geological, biological, and archeological contexts [1,2]. It is believed that the phase equilibrium of water and ice is shifted according to the Gibbs-Thomson relation [3] (Figure 1). However, owing to the small and complex geometrical nature of porous materials, the local phase equilibrium in nanoconfinement remains unresolved. Direct imaging of freezing can provide local mechanistic information on water-ice phase equilibrium and crystallization dynamics under confinement. Herein, we demonstrate the unique opportunity of observing confined phase equilibrium in a MEMS high aspect ratio nanochannel array with *in situ* phase contrast enhancement enabled by a silicon nitride (Si_3N_4) dielectric mirror [4] (Figure 2).

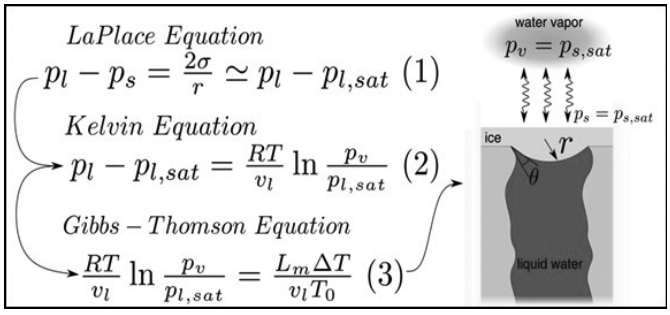

Figure 1: Liquid water in a pore can coexist, metastably, with ice and an unsaturated vapor. Capillarity between liquid and ice (Laplace) places the liquid under tension and allows for phase equilibrium (Kelvin) with the liquid under tension. This equilibrium can be expressed as the Gibbs-Thomson equation.

Fabrication and Experiment. The device fabrication process can be summarized as follows: A LPCVD Si_3N_4 layer of ~ 200 nm thickness was first deposited on a silicon wafer followed by a PECVD layer of silicon oxide with thickness corresponding to the desired channel height. Nanochannel patterns were then transferred and patterned via photolithography. The channels were formed by etching the oxide layer with 30:1 buffered oxide etch (BOE).

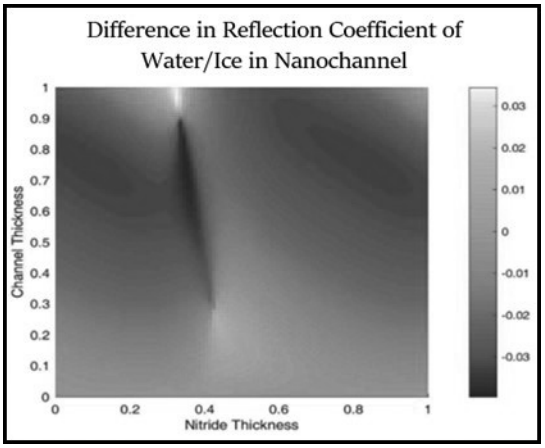

Figure 2: Calculated difference in the reflection coefficient of water and ice in the nanochannels, with axes normalized to incident wavelength. The maximum difference is found with nitride thickness in between 0.4 and 0.5, which for visible light correlates to a nitride thickness of 130 nm-260 nm. This difference is insensitive to channel thickness.

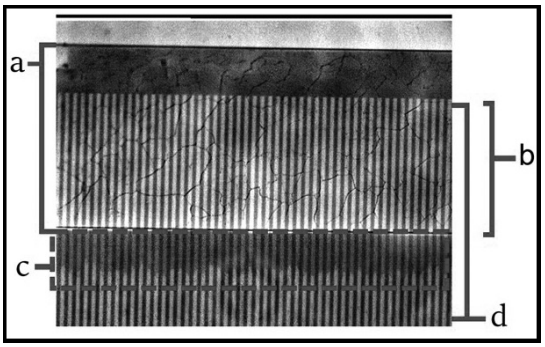

Figure 3, top: Image obtained from freezing experiment. (a) Microchannel containing bulk ice, identified by the grain boundaries present in image. (b) 500 μm channel overlap. (c) Liquid water in nanochannels (darker region) coexisting with ice (brighter region) at subfreezing temperature. (d) Nanochannel array.

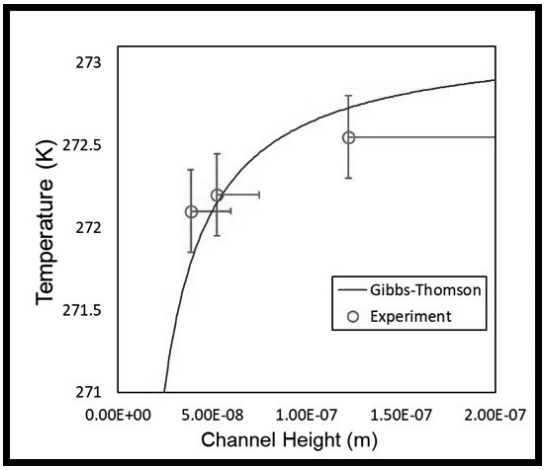

Figure 4, bottom: Melting temperatures of ice in nanochannels with different channel heights compared to the Gibbs-Thomson prediction. Values agree with those predicted by the Gibbs-Thomson relation.

For the glass wafer, a 250 nm PECVD amorphous silicon (α-Si) layer was deposited and annealed as an etch mask. Photolithography was then used to transfer the pattern of microchannels. SF_6/O_2 reactive ion etch in the Oxford 80 etcher was used to pattern the α-Si etch mask and the 10 μm microchannels were etched in 49% hydrofluoric acid.

When complete, the patterned silicon and glass wafers were aligned and anodically bonded using the MA6-BA6 contact aligner and SÜSS SB8e substrate bonder. The bonded wafers were diced and microchannel inlets were cut out with the VersaLaser.

For testing, individual devices were placed in an environmental chamber with pressure and temperature regulation. Water vapor was then pumped through the chamber to fill the nanochannels with liquid water upon capillary condensation, from which the channel height was deduced. The microchannels were filled by condensation by further raising the vapor pressure to saturation. Once filled, the chamber temperature was lowered to initiate freezing in the nanochannels and confined phase equilibrium was captured with a CCD camera positioned above the chamber. The nanoconfined water-ice phase equilibrium was successfully captured as shown in Figure 3. The melting temperatures of confined ice were reported in Figure 4 and were consistent with the Gibbs-Thomson prediction.

Conclusions:

A microfluidic device consisting of high aspect ratio nanochannels was fabricated. A layer of ~ 200 nm Si_3N_4 was deposited underneath the channels, resulting in detectable contrast between the liquid water and ice in the channels. The melting temperatures of confined ice agreed with the Gibbs-Thomson relation. Continued work will focus on studying the transport dynamics of ice-water in confinement.

Acknowledgements:

Professor Abraham Stroock, Hanwen Lu, Melanie-Claire Mallison, CNF REU Program Coordinators, and CNF Staff. This work was completed in part at the Cornell NanoScale Science and Technology Facility, an NNCI member, which is supported by the NSF (Grant No. ECCS-1542081). This work was supported in part by a grant from the Air Force Office of Scientific Research (FA9550-18-1-0345).

References:

[1] Bartels-Rausch, T., et al. "Ice structures, patterns, and processes: A view across the icefield." Rev. Mod. Phys. 2012, 84, 885.

[2] Wettlaufer, J., et al. "Premelting Dynamics." Annu. Rev. Fluid Mech., 2006, 38, 427-452.

[3] Liu, Z., et al. "Measurement of freezing point depression of water in glass capillaries and the associated ice front shape." Phys. Rev., 2003, 67, 6.

[4] Li, H., et al. "Direct visualization of fluid dynamics in sub-10 nm nanochannels." Nanoscale, 2017, 9, 9556.

Nanosecond Spin-Orbit Torque Switching of Three Terminal Magnetic Tunnel Junctions with Low Write Error Rate

CNF Project Number: 111-80

Principal Investigator: Robert A. Buhrman

User: Shengjie Shi

Affiliation: Applied and Engineering Physics, Cornell University

Primary Source of Research Funding: Department of Defense-Intelligence Advanced Research Projects Activity

Contact: buhrman@cornell.edu, ss2882@cornell.edu

Primary CNF Tools Used: ASML, JEOL 6300 e-beam, Veeco AFM

Abstract:

Recently we reported that a significant reduction of critical switching current I_c can be achieved in tungsten-based three-terminal magnetic tunnel junctions with atomic Hf layer modification of the interfaces. This has stimulated additional work to further optimize these nanoscale structures to achieve still lower critical currents and higher speed switching for future cache memory applications. Here we report on a systematic study of the micromagnetic factors that determine both the intrinsic time scale of this nanosecond switching behavior and the degree of symmetry between the fast switching from parallel (P) to anti-parallel (AP) and the reverse. Using a modified geometry of the nanopillar magnetic tunnel junction structure we find that we are able to tune the relative speeds of reversal between two polarities. We have also designed a new spin Hall channel geometry to achieve a major reduction in channel resistance. This enables us to examine write error rates in the very high pulse current regime, $I >> I_c$. (See Figure 1.) The results of these studies further demonstrate the feasibility of this type of three-terminal spin-orbit torque device as a high speed, energy efficient, non-volatile memory solution.

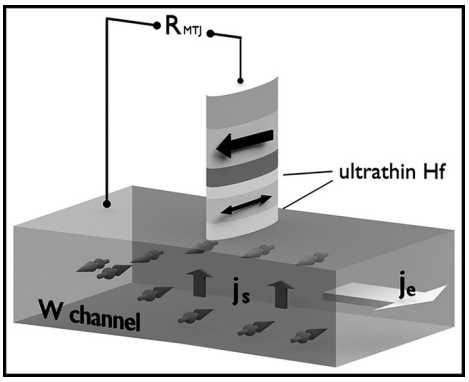

Figure 1: Schematic picture of the three terminal MTJ and measurement technique.

Summary of Research:

One of the key advances in magnetic memory technologies is the utilization of the giant spin Hall effect to switch a nanomagnet free layer in a magnetic tunnel junction (MTJ) structure. While different areas of application set different standard for what an efficient memory cell should perform, faster operation with lower energy consumption is always desired. Three-terminal MTJs are good candidates for next generation memory application due to non-volatility and zero read disturbance characteristics. However, lower write current and faster (<1ns) write time are required for them to replace existing techniques. We have shown that with interface modification we can achieve very low write current using a tungsten-based MTJ structure with atomic layer of Hf "spacer" and "dusting" [1]. Here we demonstrate high speed operation of these nano-structures.

We fabricate a series of MTJ pillars on top of 4 nm of PtHf alloy spin Hall channels. We show that we can achieve fast pulse switching with characteristic time scale smaller than 1 ns (Figure 2 and Figure 3), and the write error rate can be driven down below 10^{-6}, with high enough overdrive in the spin Hall channel. This extraordinary performance could potentially be due to fast domain nucleation process induced by various factors including Oersted field / field like torque / sample geometry.

Micromagnetic simulation shows that non-uniform initial state can be beneficial to switching, promoting switching speed in a preferred direction [2].

Our research shows that if we can utilize (or control) preferred non-uniform configuration and it is possible to achieve ultra-fast pulse switching in the MTJs.

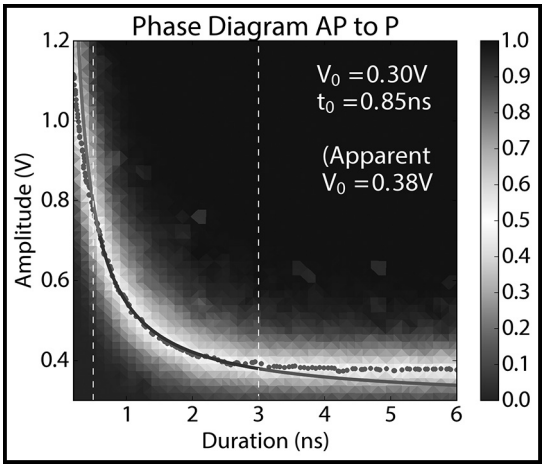

Figure 2: Switching probability of the free layer with injection of voltage pulses at various durations. Switching polarity is from AP to P.

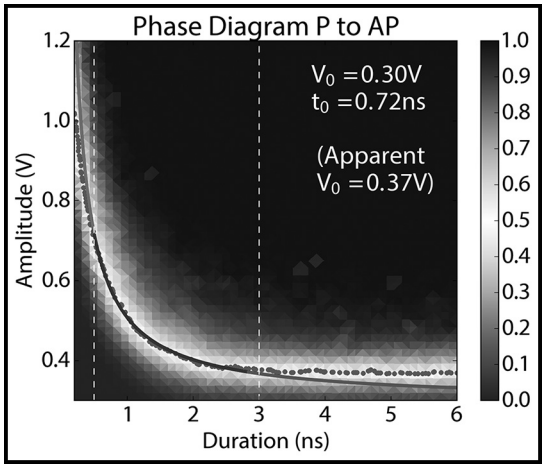

Figure 3: Switching probability of the free layer with injection of voltage pulses at various durations. Switching polarity is from P to AP.

References:

[1] Shengjie Shi, Yongxi Ou, S. V. Aradhya, D. C. Ralph and R.A. Buhrman, Fast Low-Current Spin-Orbit-Torque Switching of Magnetic Tunnel Junctions through Atomic Modifications of the Free-Layer Interfaces. Phys. Rev. Applied. 9, 011002 (2018).

[2] Aradhya, S. V., Rowlands, G. E., Oh, J., Ralph, D. C. and Buhrman, R. A. Nanosecond-Timescale Low Energy Switching of In-Plane Magnetic Tunnel Junctions through Dynamic Oersted-Field-Assisted Spin Hall Effect. Nano Lett. 16, 5987-5992 (2016).

Reduction of the Spin Hall Angle in Oxygen-Doped Beta Tungsten

CNF Project Number: 111-80

Principal Investigator: Robert A. Buhrman

User: Ryan Tapping

Affiliation: Applied and Engineering Physics, Cornell University

Primary Source of Research Funding: The Office of Naval Research and the National Science Foundation

Contact: buhrman@cornell.edu, rct76@cornell.edu

Primary CNF Tools Used: GCA 5x stepper, AJA sputtering tool, Veeco Icon AFM

Abstract:

Spintronic devices rely on spin currents that can be generated from charge currents flowing through certain non-magnetic metals. The spin Hall angle (SHA) is a measure of a materials' efficiency of this charge to spin current conversion. Tungsten is useful because the thin films have been shown to have a very large SHA of over 0.30, but only when the tungsten is ordered in the A15 structure (β-W) [1]. It has been previously shown that incorporation of oxygen into the tungsten during deposition can promote β-W growth and increase the SHA. Using spin-torque ferromagnetic resonance (ST-FMR) [2], we demonstrate that the SHA may actually decrease from over 0.30 to 0.10 or less as the oxygen concentration increases. We also show that the roughness of the tungsten films is approximately 0.19 ± 0.03 nm and is not significantly affected by the oxygen incorporation.

Summary of Research:

Thin film samples were deposited onto 100 mm silicon wafers using our magnetron sputtering system. The structure was W(8)/$Fe_{60}Co_{20}B_{20}$(t_{FeCoB})/MgO(2)/Ta(1) with numbers in parenthesis representing the thickness of the layer in nanometers, and t_{FeCoB}, the thickness of FeCoB, was varied between 2 and 4 nm. Oxygen was incorporated only during the sputtering of tungsten, with the percentage corresponding to the relative amount of oxygen to argon. Stacks were then patterned into 20 × 5 μm^2 microstrips using photolithography with the 5X g-line stepper at CNF and etched using our own ion milling system. The contacts were made using the AJA sputtering system at CNF. An optical image of the microstrip is shown in Figure 1.

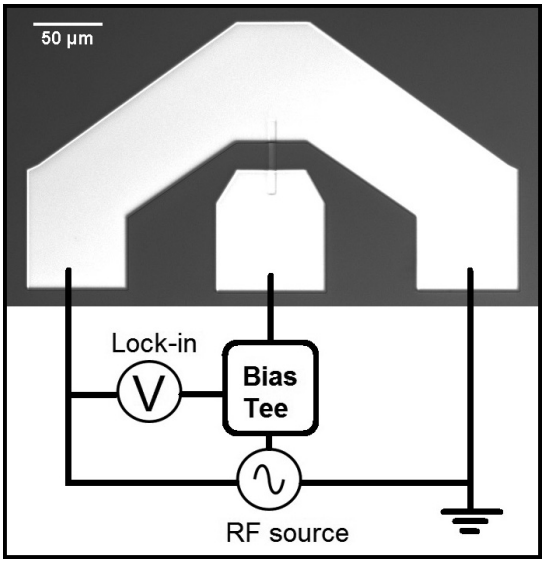

Figure 1: Microstrip after fabrication with a schematic of the ST-FMR measurement.

X-ray diffraction measurements were done on the tungsten thin films to verify that the sputtering techniques yielded β-W. Peaks were found corresponding to mostly β phase tungsten composition, and with some mixed phase α-W likely present. Resistivity measurements, using the van der Pauw method, also confirmed that the films were majority β phase, where β-W typically has a resistivity of between 100-300 $\mu\Omega$·cm [1]. Resistivities ranged from 127 $\mu\Omega$·cm for tungsten films with no oxygen incorporation to 329, 306, and 723 $\mu\Omega$·cm for tungsten with 1.6%, 2.4% and 4.0% oxygen respectively.

The spin hall angle (SHA) was determined using spin-torque ferromagnetic resonance (ST-FMR) with analysis described by Pai, et al., for determination of the SHA [2]. This technique works by driving a microwave frequency (RF) current through the microstrip, which induces magnetic precession in the ferromagnetic layer via the spin transfer torque. A magnetic field is swept from -3000 to 3000 Oe at 45° to the microstrip and the voltage

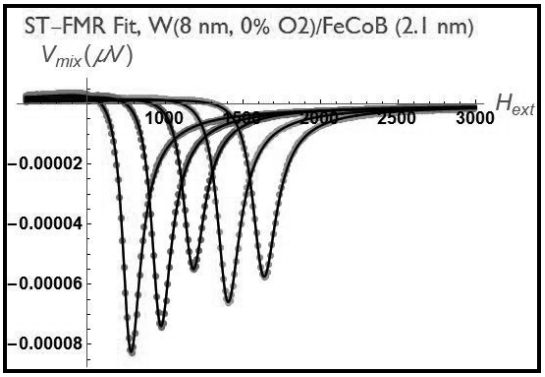

Figure 2: Voltage output from a magnetic field sweep from ST-FMR. Fits are also shown at 8, 9, 10, 11, and 12 GHz frequencies.

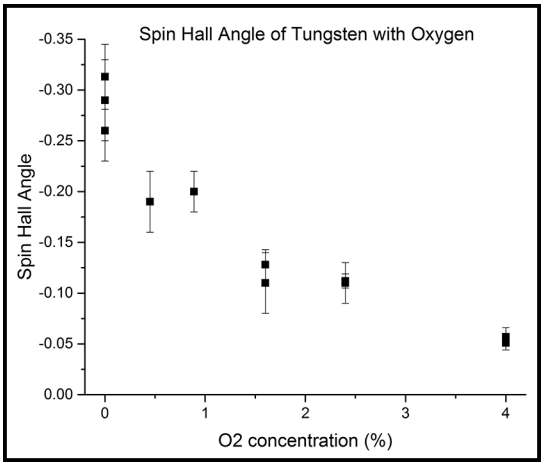

Figure 3: The spin hall angle (SHA) vs. oxygen incorporation in tungsten films.

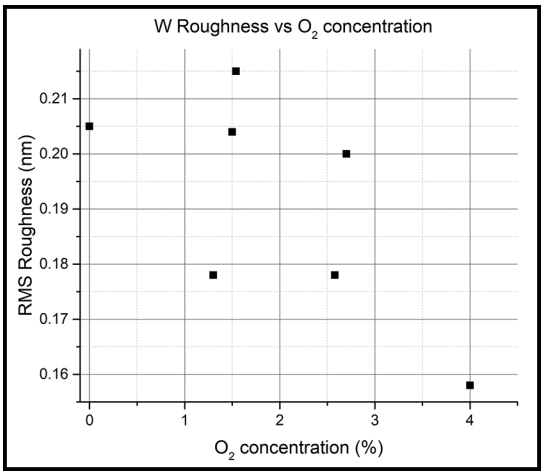

Figure 4: The roughness of tungsten films vs. oxygen incorporation shows no significant variation.

is measured by a lock-in amplifier, then the measurement is repeated for various frequencies. A lineshape analysis is done by fitting a Lorentzian function with symmetric (S) and antisymmetric (A) components as shown in Figure 2. The ratio of the prefactors S and A yield ξ_{FMR}, the spin torque efficiency. By fitting $1/\xi_{FMR}$ vs. $1/t_{FeCoB}$, the SHA is extrapolated.

For pure tungsten films with no oxygen incorporation, the SHA was found to be 0.31 ± 0.03. However, as oxygen incorporation increased, the SHA was found to decrease, with values of 0.13 ± 0.02 and 0.06 ± 0.01 for tungsten with 1.6% and 4.0% oxygen respectively. The results of the SHA vs. oxygen incorporation for several samples are shown in Figure 3. Despite resistivity data demonstrating potentially enhanced β-W growth, the SHA reduces as oxygen is incorporated. The roughness of pure tungsten films with varying oxygen concentration were measured using the Veeco Icon AFM at CNF and all films had an rms roughness of 0.19±0.03 nm, independent of oxygen concentration, as shown in Figure 4.

An explanation for the reduction in the SHA may be that the pure tungsten films were already grown in the β phase, and thus adding oxygen could not enhance the growth further. Rather, the oxygen may have only oxidized the tungsten which would also explain the increase in resistivity. This result contradicts the findings of K. Demasius, et al., which showed an enhancement of the SHA with oxygen incorporation [1].

References:

[1] Kai-Uwe Demasius, Timothy Phung, Weifeng Zhang, Brian P. Hughes, See-Hun Yang, Andrew Kellock, Wei Han, Aakash Pushp, and Stuart S.P. Parkin, Nat. Comm. 7, 10644 (2016).

[2] Chi-Feng Pai, Yongxi Ou, Luis Henrique Vilela-Leão, D.C. Ralph, and R.A. Buhrman, Phys. Rev. B. 92, 064426 (2015).

Study of Spin-Orbit Torques in Transition Metal Dichalcogenide / Ferromagnet Heterostructures

CNF Project Number: 598-96

Principal Investigator: Daniel C. Ralph

User: Vishakha Gupta, Gregory Stiehl, Ruofan Li

Affiliation: Physics, Cornell University

Primary Source of Research Funding: DOE Office of Science

Contact: DCR14@cornell.edu, VG264@cornell.edu, GMS263@cornell.edu, RL643@cornell.edu

Primary CNF Tools Used: AFM Veeco Icon, Zeiss Supra SEM and Nabity, SC4500 even hour evaporator, Oxford 81 etcher, AJA sputter deposition

Abstract:

Two-dimensional (2D) transition metal dichalcogenides (TMDs) present a unique platform for spintronics because of their strong spin-orbit (S-O) couplings and atomically flat surfaces which can be readily interfaced with other materials. Our focus is the study of TMDs coupled to ferromagnets, which can lead to the generation of novel spin-orbit torques. Fabrication of these heterostructures requires special techniques to ensure that their interface remains clean and well-ordered throughout. We discuss the methods for fabricating TMD/ferromagnet devices and present electrical measurements that measure the spin-orbit torques produced.

Summary of Research:

Recent experiments have demonstrated that integrating a ferromagnetic material with a low symmetry crystalline material that possesses strong spin-orbit (S-O) coupling can generate new forms of S-O torques, which can be used to efficiently manipulate magnetic devices with perpendicular magnetic anisotropy [1,2]. Single-crystal transition metal dichalcogenides (TMDs) are a family of layered materials with strong S-O coupling that have a wide variety of crystal symmetries [3]. This makes them ideal candidate spin source materials for the generation of novel S-O torques. Here, we discuss methods to assemble heterostructures of exfoliatable TMDs (like WTe_2, $TaTe_2$, $MoTe_2$, $NbSe_2$) and thin metallic ferromagnets for making quantitative measurements of the various torques generated.

The layers in a TMD crystal are bonded by weak van der Waal interactions and can be easily isolated by mechanical cleaving. We fabricate our samples by exfoliating the TMD from a bulk crystal using the scotch tape method, onto a high resistivity silicon wafer. The final step of the exfoliation process is carried out under high vacuum ($< 10^{-6}$ torr). This prevents degradation of the atomically flat TMD surface through absorption of water vapor and/or oxygen.

The TMD is interfaced with 6 nm of permalloy (Py = $Ni_{81}Fe_{19}$), which is deposited by grazing-angle DC magnetron sputtering (with a rate < 0.2 Å/s) to minimize mechanical damage to the TMD surface. To prevent oxidation of the ferromagnet, the sample is further capped with 2 nm of aluminum. A combination of optical microscopy and atomic force microscopy (CNF AFM Veeco Icon) are used to identify thin (< 15 nm) and homogenous (surface roughness < 300 pm) regions on TMD flakes (Figure 1).

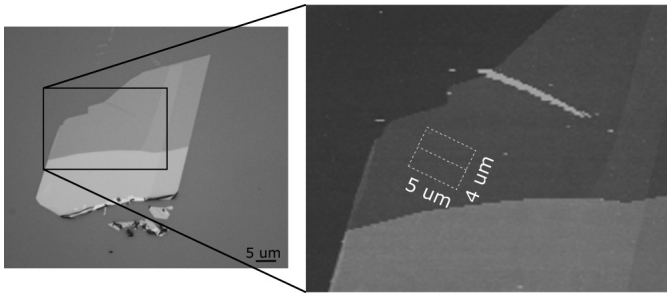

Figure 1: (left) Optical image of TMD/Py sample on a Si substrate before device patterning. The different color intensities indicate different thicknesses. (right) AFM image of the boxed region. White dashed lines indicate the active region used to make the device, with surface roughness < 300 pm and thickness 2.2 nm.

E-beam lithography (CNF Zeiss Supra SEM, Nabity) is used to pattern the selected flakes into bar geometries of ~ 4 × 5 μm in size, needed to perform spin-torque

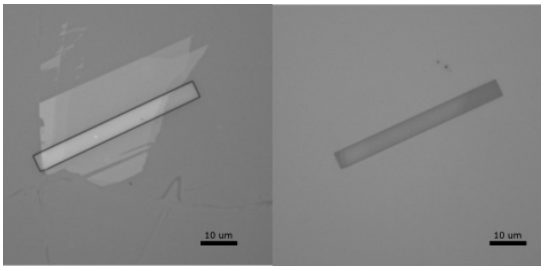

Figure 2: Optical Images of (left) Bar geometry patterned onto a TMD flake. (right) The flake around the bar is etched away using Ar ion milling. The region under the bar is protected by a hard SiO_2 mask.

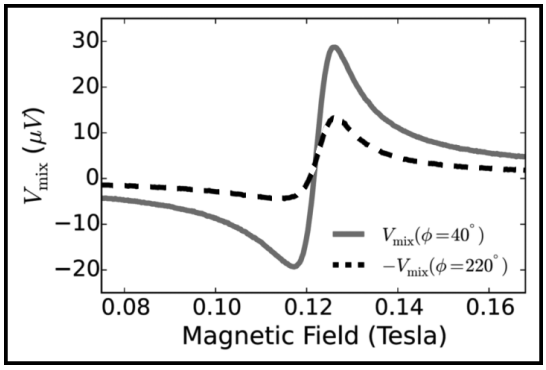

Figure 4: ST-FMR resonances for a TMD/Py sample with magnetization oriented at 40° and 220° relative to the current direction [1].

ferromagnetic resonance (ST-FMR) measurements [4,5] or second harmonic Hall measurements [6,7]. A hard mask of SiO_2 is used (CNF SC4500 even hour evaporator) to protect the active region of the device while the rest is etched out using Ar ion milling (Figure 2).

To protect the edges of the TMD/Py bilayer after ion milling, the sample is re-clamped by sputtering a thin conformal coating of SiO_2 (CNF AJA sputter deposition). A final round of e-beam lithography (CNF Zeiss Supra SEM, Nabity) is performed to make electrical contact with the defined bars. The SiO_2 mask in the contact region is removed using reactive-ion etching (RIE) with a CHF_3/Ar mixture (CNF Oxford 81 etcher). Finally, Ti/Pt (CNF AJA sputter deposition) contacts are sputter deposited through a lift-off process.

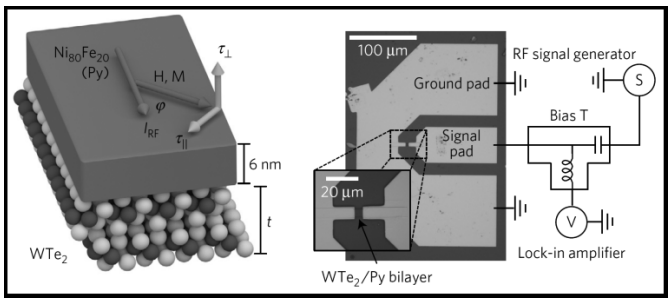

Figure 3: (left) Schematic of the heterostructure geometry [1] (right) Optical image of final device and schematic of the circuit used for ST-FMR measurements [1].

We use ST-FMR to measure the torques produced at room temperature [4,5]. As depicted in Figure 3, an RF current (8-12 GHz) is applied to the sample along with an in-plane magnetic field to tune the ferromagnet through resonance. The precessing magnetization gives rise to a changing anisotropic magnetoresistance (AMR), which mixes with the current leading to a DC signal V_{mix} that is measured (Figure 4). By analyzing the symmetric and antisymmetric components of the V_{mix} lineshape as a function of applied field, the various torque contributions can be computed [1].

In conclusion we have provided a detailed discussion of the techniques employed in fabricating TMD/ferromagnet heterostructure devices and have presented spin-torque ferromagnetic resonance data that measures the S-O torques generated. TMDs allow for a systematic study of these torques as a function of various crystal symmetries and thicknesses [2]. These investigations provide important clues towards identifying the role of broken symmetries and bulk- vs. interface-driven mechanisms in the generation of spin-orbit torques.

References:

[1] MacNeill, D. et al., "Control of spin–orbit torques through crystal symmetry in WTe_2/ferromagnet bilayers," Nature Physics 13, 300 (2017).

[2] MacNeill, David, et al., "Thickness dependence of spin-orbit torques generated by WTe_2," Physical Review B 96, 054450 (2017).

[3] Wilson, J. A., and A. D. Yoffe, "The transition metal dichalcogenides discussion and interpretation of the observed optical, electrical and structural properties," Advances in Physics 18, 193 (1969).

[4] Liu, Luqiao, et al., "Spin-torque ferromagnetic resonance induced by the spin Hall effect," Physical Review Letters 106, 036601 (2011).

[5] Liu, Luqiao, et al., "Spin-torque switching with the giant spin Hall effect of tantalum," Science 336, 555 (2012).

[6] Hayashi, Masamitsu, et al., "Quantitative characterization of the spin-orbit torque using harmonic Hall voltage measurements," Physical Review B 89, 144425 (2014).

[7] Garello, Kevin, et al., "Symmetry and magnitude of spin–orbit torques in ferromagnetic heterostructures," Nature Nanotechnology 8, 587 (2013).

Spin Hall Effect in $CaRuO_3$

CNF Project Number: 598-96

Principal Investigators: Daniel Ralph, Darrell Schlom

Users: Neal Reynolds, Hari Nair, Nathaniel Schreiber

Affiliations: Laboratory of Atomic and Solid State Physics, Materials Science and Engineering; Cornell University

Primary Source of Research Funding: National Science Foundation

Contact: dcr14@cornell.edu, schlom@cornell.edu, ndr37@cornell.edu

Primary CNF Tools Used: 5x g-line stepper, AJA sputter deposition tool, Heidelberg DWL2000

Abstract:

The spin Hall effect results in the generation of pure spin current that flows transverse to an applied electric field in non-magnetic materials. Recent experimental and theoretical work has shown that the presence and evolution of heavily-renormalized, flat, quasi-particle bands near the Fermi level can dramatically influence the magnitude of the spin Hall effect. $CaRuO_3$ is a so-called "Hund's metal" in which electron correlation due Hund's rule coupling is relevant. These strong correlations along with the large octahedral distortions in $CaRuO_3$ results in the emergence of flat quasi-particle bands below 120 K and a change in sign of the Hall coefficient below ~ 50 K — indications of non-trivial modifications of the Fermi surface by the quasi-particle bands as temperature is decreased. In this report we discuss the measurement of the spin Hall effect in $CaRuO_3$/Permalloy ($Ni_{80}Fe_{20}$, Py) bilayers as a function of temperature.

Summary of Research:

The spin Hall effect arises from spin-dependent interaction with a material's band structure, so-called "intrinsic" contributions, and spin-dependent scattering off of impurities in a given material, so-called "extrinsic" contributions. Intrinsic contributions to the spin Hall effect are large when in materials with strong spin orbit coupling and when the Fermi level lies within avoided crossings opened up by the strong spin orbit coupling. Materials that are expected to have large intrinsic spin Hall effects are then the late transition metals (those with 5d valence) [1], and the f-valent lanthanides [2] and actinides. Very recent work in a rare-earth Kondo lattice system has suggested that the presence of Kondo-derived heavy quasi-particle bands near the Fermi level can drive an enhancement of the spin Hall effect. The understanding of this enhancement, however, is complicated by the fact that the Kondo physics also gives rise to an enhancement of the 4*f* orbital bands near the Fermi level, which has been shown to independently enhance the spin Hall effect [2].

To understand the contribution of the strong correlation on the enhancement of the spin Hall effect without 4*f* orbitals present, we examine the spin Hall effect in calcium ruthenium trioxygen ($CaRuO_3$) as a function of temperature, because it exhibits pockets of flat quasi-particle bands starting at 120 K and below. The evolution of the Fermi surface due to these bands culminates in a reversal of the Hall coefficient at ~ 50 K. Given the sensitivity of the intrinsic spin Hall effect to the material's band structure, we expect that as temperature is decreased from room temperature we will observe a change in the spin Hall effect at these temperatures.

$CaRuO_3$ was grown on a neodymium gallium trioxygen ($NdGaO_3$) substrate using molecular beam epitaxy (MBE) in collaboration with the Schlom group. Films were then taken to a sputter deposition system to deposit Permalloy (Py) and an aluminum capping layer. Micron-scale devices were patterned out of the films via photolithography using the 5x g-line stepper, and argon ion milling was used to define the devices. Ti/Pt liftoff leads were applied via photolithography, again with 5x g-line stepper, and the AJA sputter deposition tool. An optical image of a finished device is shown in Figure 1.

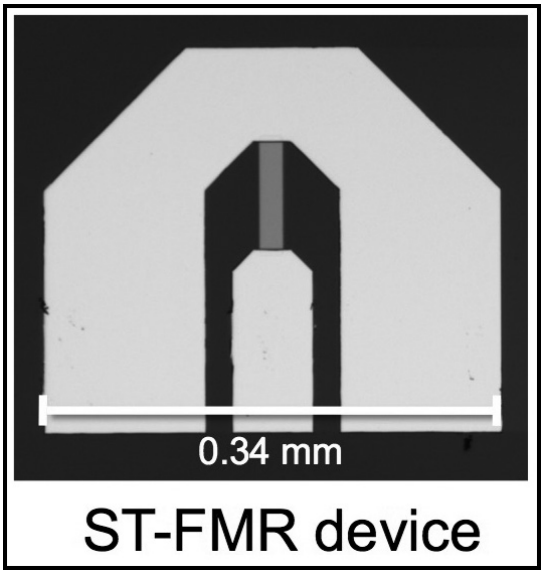

Figure 1: An optical image of a finished device used to measure the spin Hall effect via ST-FMR.

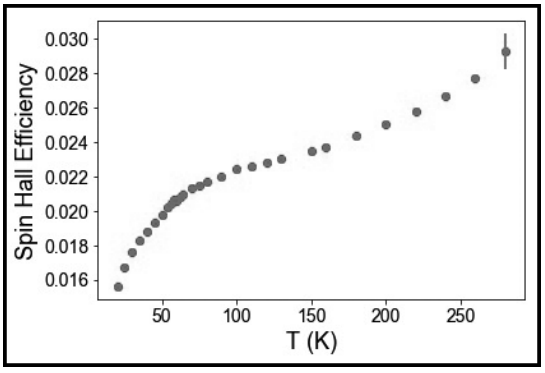

Figure 2: Spin Hall effect efficiency as a function of temperature measured by ST-FMR of a $CaRuO_3$/Py bilayer. The spin Hall effect decreases going from 280 K to 20 K with an inflection points at ~ 120 K and a slope change vs T at ~ 50 K consistent with the onset of the quasi-particle bands and the Hall effect coefficient sign reversal observed in $CaRuO_3$, respectively.

Measurements of the spin Hall effect as a function of temperature were done using spin torque-ferromagnetic resonance (ST-FMR) [3,4] in a custom He-flow cryostat. ST-FMR uses a microwave frequency signal (6-20 GHz) to excite resonant dynamics of the magnetic Py layer that then leads to a measurable voltage that is proportional to the strength of the spin Hall effect.

We report the strength of the spin Hall effect as a dimensionless efficiency calculated as the ratio of the measured spin current to applied charge current. We find a gradual decrease of the spin Hall effect with temperature, but with an inflection point ~ 120 K, consistent with the onset of the quasi-particle states, and a change in slope at ~ 50 K, commensurate with the change in Hall effect coefficient sign (Figure 2).

References:

[1] H. L. Wang, C. H. Du, Y. Pu, R. Adur, P.C. Hammel, and F. Y. Yang, Phys. Rev. Lett. 112, 197201 (2014).

[2] N. Reynolds, P. Jadaun, J. T. Heron, C. L. Jermain, J. Gibbons, R. Collette, R. A. Buhrman, D. G. Schlom, and D. C. Ralph, Phys. Rev. B 95, 064412 (2017).

[3] L. Liu, T. Moriyama, D. C. Ralph, and R. A. Buhrman, Phys. Rev. Lett. 106, 036601, (2011).

[4] L. Liu, C. F. Pai, Y. Li, H. W. Tseng, D. C. Ralph, and R. A. Burhman, Science 366, 555 (2012).

Wrapping Microdroplets with Two-Dimensional Materials

CNF Project Number: 900-00

Principal Investigators: Paul L. McEuen[1,2], Itai Cohen[1,2], Jiwoong Park[3,4]

Users: Kathryn L. McGill[1], Michael F. Reynolds[1], Marc Z. Miskin[1,2], Maritha Wang[3,4], Hui Gao[3,4], Kibum Kang[3,4]

Affiliations: 1. Laboratory of Atomic and Solid State Physics, Cornell University, Ithaca NY, USA; 2. Kavli Institute at Cornell for Nanoscale Science, Cornell University, Ithaca NY, USA; 3. Department of Chemistry and Chemical Biology, Cornell University, Ithaca NY, USA; 4. Department of Chemistry, Institute for Molecular Engineering, and James Franck Institute, University of Chicago, Chicago IL, USA

Primary Sources of Research Funding: Cornell Center for Materials Research with funding from the NSF MRSEC program (DMR-1719875), Air Force Office of Scientific Research (AFSOR) Multidisciplinary Research Program of the University Research Initiative Grant FA2386-13-1-4118

Contact: plm23@cornell.edu, klm274@cornell.edu, mfr74@cornell.edu

Primary CNF Tools Used: Autostep i-line stepper, Oxford 81 etcher

Abstract:

We present experiments demonstrating the wrapping of microscopic oil droplets by two-dimensional (2D) materials. We show that 2D materials such as graphene and molybdenum disulfide (MoS_2) wrap microscopic liquid drops in the same ways in which millimeter-scale drops were wrapped by thin elastic sheets [1,2].

Summary of Research:

Wrapping fluid droplets with thin elastic sheets has been used to perform capillary origami [3] and as a technique to measure bending moduli [4] of thin films. In the case where the bending energy of the sheet is much smaller than the surface tension of the droplet, the minimization of surface energy by wrapping and the inability for a planar sheet to take on Gaussian curvature determine the shape. Previous experiments include geometric wrapping patterns of droplets [2] and wrinkling of sheets on droplet surfaces [5]. Here we perform analogous experiments on the wrapping of oil droplets in water with the thinnest possible materials: one-atom-thick graphene and three-atom-thick MoS_2.

We begin by photolithographically patterning 2D materials into a variety of simple shapes using the GCA AutoStep 200 i-line wafer stepper and the Oxford etchers at the Cornell NanoScale Science and Technology Facility. We use commercially available graphene on copper (Grolltex) and transfer it onto glass coverslips using a poly(methyl methacrylate) (PMMA) support layer. Our MoS_2 samples are grown onto glass coverslips via metal-organic chemical vapor deposition (MOCVD) by collaborators in Jiwoong Park's group at the University of Chicago, and we cover them in a protective layer of

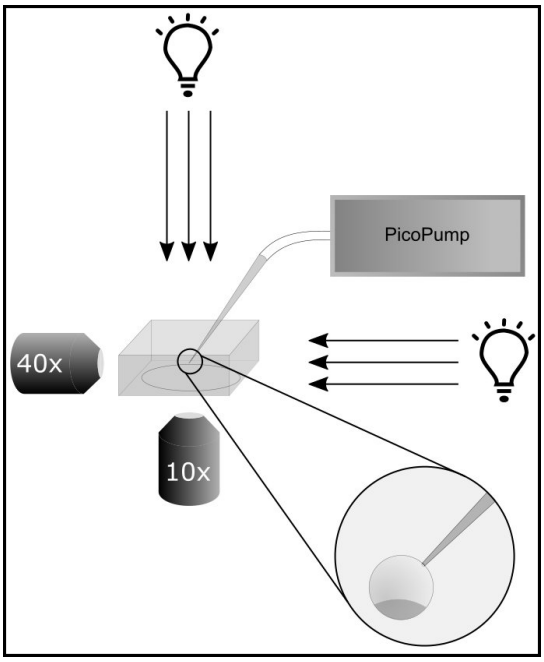

Figure 1: Schematic of setup. Inset shows Fluorinert drop with 2D material wrapping from the bottom.

PMMA during fabrication. After patterning, we etch through the PMMA/MoS_2 or graphene to define our features. We then remove the PMMA and release the graphene or MoS_2 from the glass substrate with a dilute hydrofluoric acid etch.

The experimental setup is shown schematically in Figure 1. The substrates containing the 2D material sheets are placed in a home-built cuvette filled with deionized water. Using an electronic micromanipulator (Sensapex), we position a glass micropipette filled with Fluorinert FC-70 (3M), an oil that is both denser than and index-matched to water, over the graphene/MoS_2 sheets. Droplets are formed by applying pressure spikes (Picopump, World Precision Instruments) to the micropipette, then lowered onto the 2D material sheets for pick up. We then use suction to shrink the droplet until it is completely wrapped by the 2D sheet. Simultaneously, we record the bottom and side views of the process using an inverted microscope and side-view objective, respectively.

Once we pick up the sheets, we use both the side and bottom views to simultaneously watch the wrapping process. Figure 2 shows a time series of images from both cameras as a circular MoS_2 sheet wraps a Fluorinert droplet. Frames 1 and 2 show the initial deflection of the droplet from a spherical shape due to the MoS_2 sheet. Frame 3 shows a triangular-wrapped shape, one of the typical wrapping geometries for circular sheets [2], before the shape is distorted by vacuum removal of Fluorinert in frames 5 and 6.

For circular sheets, we see triangular prisms, shown in Figure 3A, and "empanada" wrapping states. For square sheets, we see square "turnover" wrapping patterns – where the four corners are folded to the center, shown in Figure 3B. For triangular sheets, as with the circular ones, wrapping corresponds roughly to triangular prisms, shown in Figure 3C. Overall, we find that wrapping geometries are similar to those in Ref. (2) and are determined by the initial shape of the 2D material sheet.

This demonstration indicates a new route for making 3D geometries out of 2D materials by drawing on an existing literature of droplet wrapping with sheets, and it suggests the possibility of using 2D materials to perform wrapping at more complicated fluid interfaces, or to controllably form 3D microstructures. Future work includes new patterns to demonstrate capillary origami folding with 2D materials as well as wrapping droplets with devices with optical, electronic, and/or magnetic components.

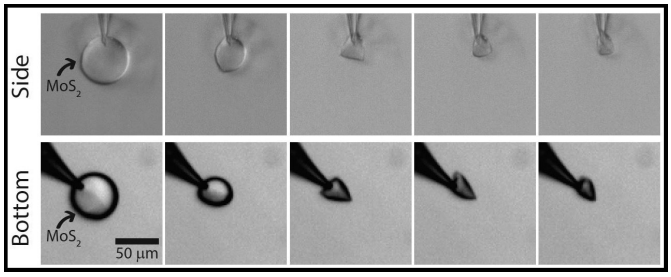

Figure 2: (top) Time lapse of Fluorinert droplet wrapping by MoS_2, side view; (bottom) Time lapse of the same droplet wrapping, bottom view.

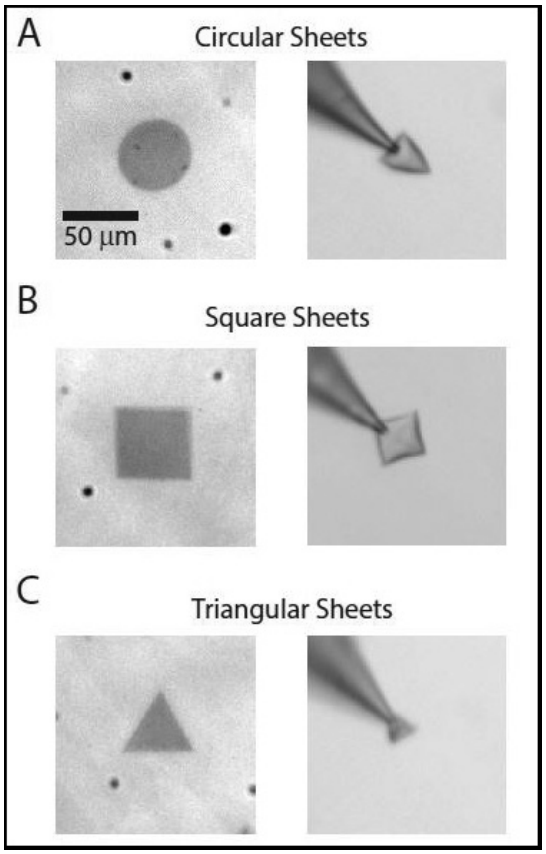

Figure 3: Final wrapped states for various sheet geometries.

References:

[1] D. Kumar, J. D. Paulsen, T. P. Russell, N. Menon, Science. 359, 775 (2018).

[2] J. D. Paulsen et al., Nat. Mater. 14, 1206-1209 (2015).

[3] G. McHale, M. I. Newton, N. J. Shirtcliffe, N. R. Geraldi, Beilstein J. Nanotechnol. 2, 145-151 (2011).

[4] J. Bae, T. Ouchi, R. C. Hayward, ACS Appl. Mater. Interfaces. 7, 14734-14742 (2015).

[5] J. Huang et al., Science. 317, 650-653 (2007).

Phase Transition and Equilibrium in Nanoconfinement

CNF Project Number: 1119-03

Principal Investigator: Abraham Duncan Stroock

User: Hanwen Lu

Affiliations: Robert Fredrick Smith School of Chemical and Biomolecular Engineering, Sibley School of Mechanical and Aerospace Engineering; Cornell University

Primary Source of Research Funding: Air Force Office of Scientific Research (FA9550-15-1-0052)

Contact: abe.stroock@cornell.edu, HL943@cornell.edu

Primary CNF Tools Used: Photolithography spinners, ABM contact aligner, Oxford 80s, P10 profilometer, general chemical hood, Zeiss Ultra scanning electron microscope (SEM), SÜSS SB8e bonder

Abstract:

Phase transitions are of natural [1,2], biological [3], and technological [4] importance. A phase transition typically takes place by nucleation catalyzed by foreign surfaces. For example, cloud formation is thought to be ice nucleation from vapor catalyzed by aerosol particles. However, due to the complex structural and chemical composition of aerosol, the exact freezing mechanism remains elusive and the lack of understanding significantly hinders our ability in predicting global radiation budget [5]. It has been proposed that nanoporous surfaces give rise to a two-step freezing process known as Pore Condensation Freezing (PCF) [6], yet the freezing transition on well-defined nanoscale roughness has not been systematically studied. Taking advantage of the nanofabrication capability at CNF, we have tackled this problem with two distinct approaches: 1) we fabricated a geometrically well-defined nanoporous membrane with Block Co-polymer (BCP) nanolithography to investigate of collective influence of nanoscopic surface topography; and 2) we fabricated high aspect ratio nanochannels via conventional lithography to directly observe phase transition in individual nanoconfinement.

Summary of Research:

Block Co-Polymer (BCP) Silicon Oxide Membrane. BCP nanolithography is a newly developed process in CNF by CNF Fellow Alex Ruyack and staff Vince Genova. BCP lithography pattern formation relies on phase separation in forming nanoscopic lamella phase aligned perpendicular to the substrate. We first spin-coated 100 nm SiO_2 PECVD film with 2% P8205-PMMA BCP. The polymer was allowed to phase separated in vacuum furnace overnight, then the PMMA is cleaved and removed leaving a coating of PS polymer with nanoscopic hollow cylinders. The porous pattern was transferred onto the substrate with plasma etching, forming a nanoporous membrane shown in Figure 1. The membrane fabricated with BCP lithography is highly mono-dispersed with typical pore radius of 13-15 nm.

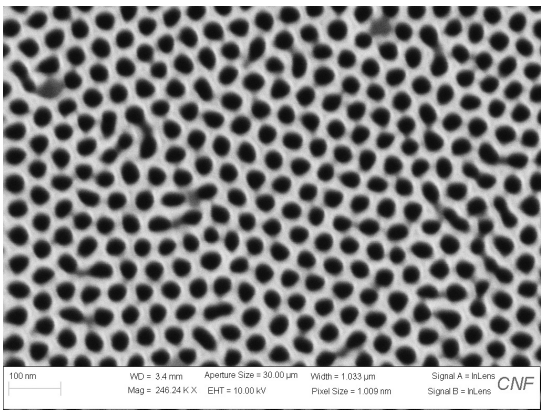

Figure 1: SEM image of BCP silicon oxide membrane. well-ordered mono-dispersed pores can be seen from a top view.

The freezing efficiency of the membrane was characterized in an environmental vacuum chamber in the Stroock lab. Figure 2 reports the temperature and saturation with respect to ice (SRI) at which freezing was initiated on the membrane. The freezing behavior on the membrane first followed the liquid saturation line and then transitioned to the capillary condensation line at around 240K. This behavior is in quantitative agreement with prediction by Pore Condensation Freezing and Classical Nucleation Theory.

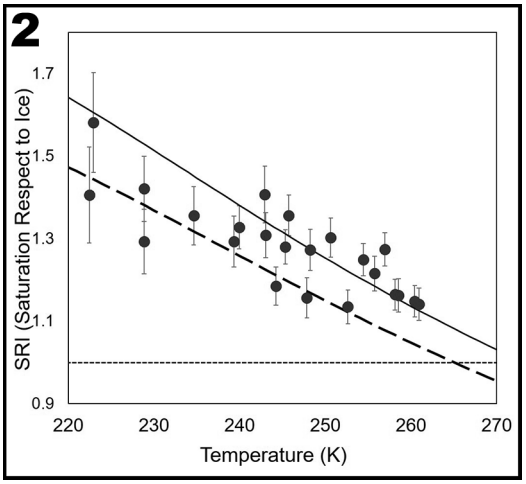

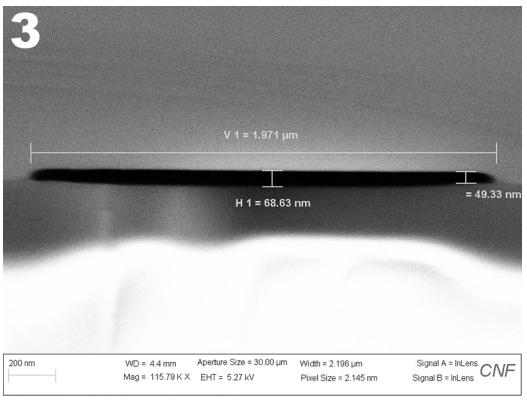

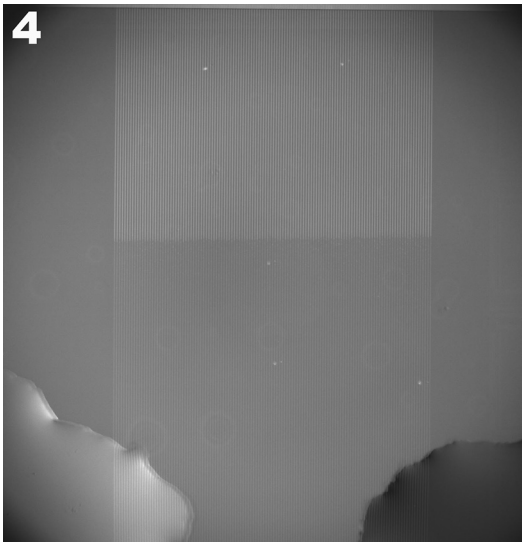

Figure 2, top: *The onset of freezing transition on BCP silicon oxide membrane. the solid is the saturation line for supercooled liquid; the dotted line is the ice saturation line; the dashed line is the capillary condensation line above which supercooled liquid can capillary condense in the nanopores. The PCF predicts that freezing follows the capillary condensation line in lower temperature catalyzed by condensed liquid in the nanopore. In the figure, freezing transitioned from the liquid saturation to the capillary condensation line at around 240K. The transition temperature predicted by Classical Nucleation Theory is 243K.* ***Figure 3, middle:*** *SEM of a cleaved nanochannel cross-section. The top side of the nanochannel is the silicon side and the bottom is the Borofloat glass.* Figure 4, bottom: *The wetting front of 10 µm nanochannel array in water. The brighter portion of the channel towards the top is dry, the darker portion is filled. The lower left/right puddle is water on top of the device.*

High Aspect Ratio Nanochannel. To experimentally study nucleation in single nanopore, we fabricated high aspect ratio nanochannels on silicon substrates. The micron-wide channel allows direct optical observation while the nanoscopic channel depth induces confinement effect that is distinctive from bulk phenomenon. The fabrication process is as follows; the nanochannel pattern was first created by conventional photolithography, then the substrate is etched in Oxford 80s in CF_4 plasma to create trenches ranging from 30 nm to 120 nm, the cross-sectional profile is then characterized with P10 profilometer as well as with Veeco Icon atomic force microscopy (AFM). Finally, nanochannels were anodically bonded to Borofloat glass to form a nanochannel microfluidic device. The cross-section of a bonded device with 2 μm width is shown in Figure 3.

Some variations of channel depth can be observed as well as large side wall slope short etching duration. Imbibition experiments were performed with the nanochannel devices. The wetting dynamics in nanochannels follows Washburn dynamics, i.e.: $L^2 = Dt$, where L is the wetting front position, t is time and D is a constant related to channel height. The imbibition dynamics in all experiment follows above relation with implied channel height consistent with SEM micrograph, with exception of the initial imbibition experiment. The faster dynamics is observed during the first imbibition which can be interpreted as result of flow in prewetting films and corners in prefect wetting scenario.

As experiments were repeated, the hydrophilicity of channel wall deteriorated and thus corner flow cannot be sustained. Crystallization and freezing phenomena in confinement are current being studied with these nanochannel devices.

References:

[1] Bartels-Rausch, T. Ten things we need to know about ice and snow. Nature 494, 27 (2013).

[2] Murray, B. J., O'Sullivan, D., Atkinson, J. D. and Webb, M. E. Ice nucleation by particles immersed in supercooled cloud droplets. Chem. Soc. Rev. 41, 6519 (2012).

[3] Mazur, P. Cryobiology: The Freezing of Biological Systems. Science (80-.). 168, 939-949 (1970).

[4] Bartels-Rausch, T. et al. Ice structures, patterns, and processes: A view across the icefields. Rev. Mod. Phys. 84, 885-944 (2012).

[5] Myhre, G. et al. Anthropogenic and Natural Radiative Forcing. Clim. Chang. 2013 Phys. Sci. Basis. Contrib. Work. Gr. I to Fifth Assess. Rep. Intergov. Panel Clim. Chang. 659-740 (2013). doi:10.1017/ CBO9781107415324.018

[6] Marcolli, C. Deposition nucleation viewed as homogeneous or immersion freezing in pores and cavities. Atmos. Chem. Phys. 14, 2071-2104 (2014).

Vortex Dynamics in Nanofabricated Superconducting Devices

CNF Project Number: 1314-05

Principal Investigator: Britton L.T. Plourde

Users: Kenneth Dodge, JJ Nelson

Affiliation: Department of Physics, Syracuse University

Primary Source of Research Funding: Army Research Office

Contact: bplourde@syr.edu, krdodgej@syr.edu, jjnelson@syr.edu

Website: http://plourdelab.syr.edu

Primary CNF Tools Used: ASML 300C DUV stepper, JEOL 9500, Plasma-Therm PT740

Abstract:

We fabricate superconducting microwave devices for studying the dynamics of vortices and quasiparticles at low temperatures. Vortices are quantized bundles of magnetic flux that thread many different superconductors over a particular range of applied magnetic field. Our experiments are aimed at investigating loss mechanisms that can limit the performance of superconducting circuits for quantum information processing. In addition, we are probing the microwave properties of various superconducting materials for future implementations of qubits.

Summary of Research:

Superconducting microwave circuits play an important role in quantum information processing. Circuits composed of Josephson junctions and capacitors with superconducting electrodes can serve as qubits, the fundamental element of a quantum computing architecture. Various loss mechanisms limit the ultimate performance of these devices, including trapped magnetic flux vortices. Vortices can be trapped in the superconducting electrodes when background magnetic fields are present and contribute dissipation when driven with microwave currents [1]. Thus, techniques for controlling the trapping of vortices are critical to the development of large-scale quantum information processors with superconducting circuits. In addition, investigations of microwave vortex dynamics can be a useful tool for probing new superconducting materials for use in future implementations of qubits.

We are fabricating a system of microwave resonators using a variety of superconducting thin films, including Nb, TiN, NbTiN, and disordered Al, for studying the loss contributed by trapped flux in these materials over the frequency range from 1.5-11 GHz [2]. By cooling the resonators in different magnetic fields, we are able to probe the loss from vortices as a function of field at the resonance frequencies contained in our design. We study the microwave properties of the vortex response as a function of various parameters, including temperature, frequency, device geometry, and film disorder.

We fabricate our microwave resonators from various superconducting films, including aluminum, deposited onto silicon wafers in vacuum systems at Syracuse University or by collaborators at other institutions. We define the patterns on the ASML stepper and transfer them into the films with a combination of reactive ion etching and wet-etch processing. We measure these circuits at temperatures of 100 mK and below in our lab at Syracuse University.

References:

[1] Song, C., Heitmann, T.W., DeFeo, M.P., Yu, K., McDermott, R., Neeley, M., Martinis, John M., Plourde, B.L.T.; "Microwave response of vortices in superconducting thin films of Re and Al"; Physical Review B 79, 174512 (2009).

[2] Dodge, K., Nelson, J., Senatore, M., Xu, P., Osborn, K., Pappas, D., Plourde, B.; "Microwave Response of Vortices in Superconducting Resonators with High Kinetic Inductance"; Bull. Am. Phys. Soc. 2018, http://meetings.aps.org/Meeting/MAR18/Session/Y39.11.

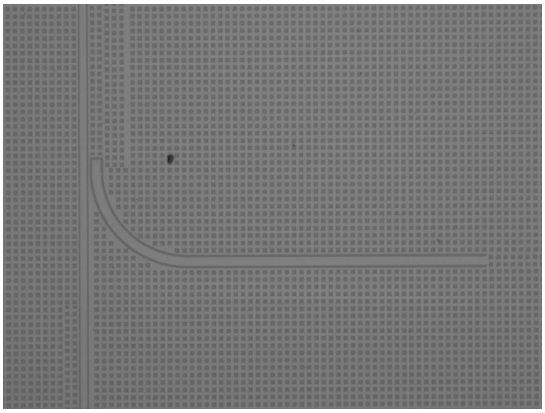

Figure 1: Coplanar waveguide resonator for probing microwave losses and magnetic field dependence in disordered superconducting aluminum thin films.

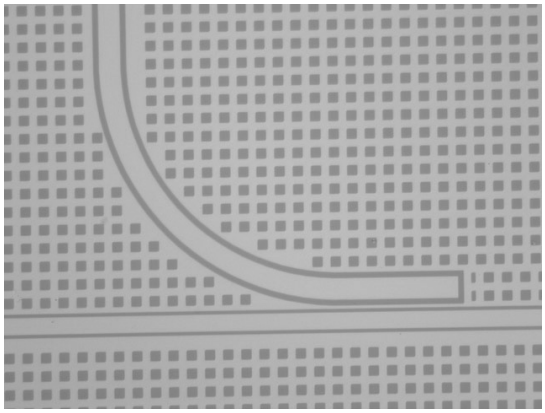

Figure 2: Capacitive coupling elbow structure for measurement of superconducting microwave resonator.

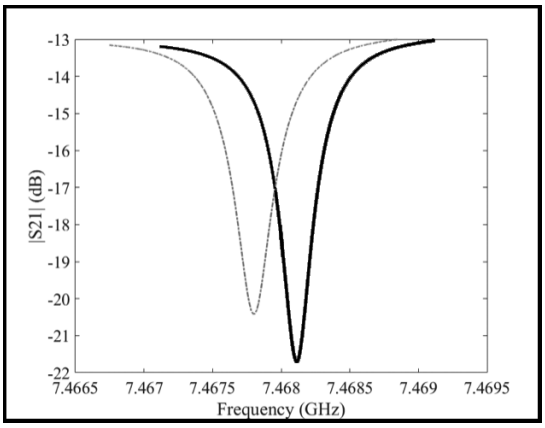

Figure 3: Measurement of microwave transmission dips corresponding to resonator patterned from disordered superconducting aluminum thin film; black (grey) curve corresponds to measurement in zero magnetic field (194 μT).

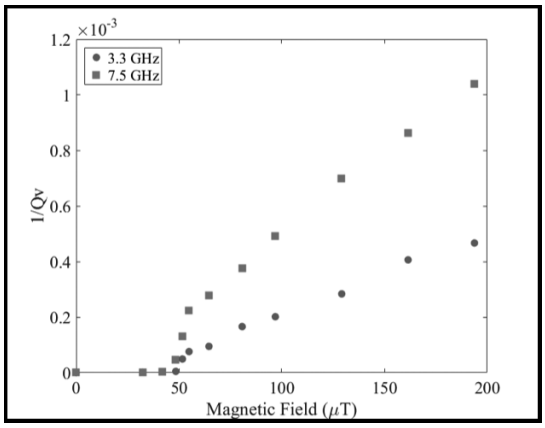

Figure 4: Microwave loss contribution from trapped vortices as a function of magnetic field in resonators patterned from disordered superconducting aluminum thin film for two different resonance frequencies.

Fabrication of Nanofluidic Cavities for Superfluid ^{3}He Studies

CNF Project Number: 1520-07

Principal Investigator: Jeevak M. Parpia

Users: Abhilash Thanniyil Sebastian, Nikolay Zhelev, Roberto DeAlba

Affiliation: Department of Physics, Cornell University

Primary Source of Research Funding: National Science Foundation

Contact: jmp9@cornell.edu

Website: http://parpia.lassp.cornell.edu

Primary CNF Tools Used: Furnaces, Oxford PECVD, contact photolithography, Oxford RIE, Plasma-Therm RIE, Unaxis DRIE, critical point dryer

Abstract:

We demonstrated nanoscale cavities that withstand 30 bar cooled to ultralow temperatures [1]. The surfaces of silicon-glass cavities are pristine having AFM characterized roughness under 1 nm [1,2]. We also examined the resonant properties of single layer graphene structures above and below room temperature. Despite extensive cleaning, there is evidence of residual polymer coatings on the surface [3].

Summary of Research:

Superfluid ^{3}He is a unique system for study. ^{3}He is a Fermion (like electrons), but its pairing into the superfluid state is more complex than its electronic counterparts producing a multiplicity of superfluid phases. In the bulk, the anisotropic A phase and the isotropically gapped B phase emerge. Confinement favors the A phase over the B phase [2,4].

The superfluid state is attained between 0 and 35 bar and between 0.9 and 2.5 mK (respectively). Below the superfluid transition, pairs condense into the coherent superfluid state. The pairing length-scale (pair diameter) varies from ~ 80 nm at 0 bar to 14 nm at high pressure. Confinement alters the phase diagram and as the ^{3}He is progressively restricted to smaller sizes, the B phase should yield to the A phase and new phases should emerge.

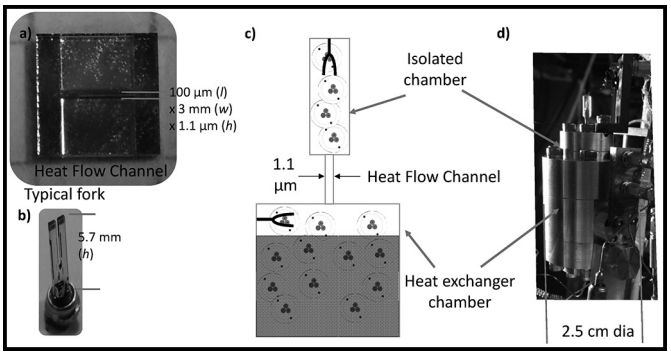

Figure 1: A. The bonded heat flow channel (5 mm square) with dimensions alongside. B. Typical quartz fork. C. Schematic of experiment. D. Photograph of experimental chamber [5]. See full color version on pages xxviii-xxix.

In one series of experiments [5], we explore the thermal conductivity of confined ^{3}He. Two chambers are separated by a micromachined channel of dimensions 3 mm × 100 μm × 1.1 μm (Figure 1a). To fabricate this channel, 1 mm thick silicon wafers were oxidized using the oxide furnace in CNF to grow thick oxide (> 2 μm), then further oxide was deposited using the Oxford PECVD. Long channels with a width of 3 mm were patterned using contact photolithography and the oxide within them removed using both dry plasma etch (Oxford and Plasma-Therm RIE) and wet etch (6:1 BOE). Wafers were further oxidized to create a step in the Si-SiO_2 interface (modified LOCOS process) and oxide removed using HF. To define the channels further laterally to 100 μm × 3 mm, a second contact lithography step was used and the exposed Si was etched using the Unaxis DRIE to 200 μm depth. After removal of masking oxide, resist, and Bosch polymer, wafers were further oxidized with an oxide film target of 300 nm to protect surface during dicing and then diced using CNF's dicing saw. Matching glass pieces were also diced. Final step is to make the cells was to remove oxide off Si pieces, clean in SC-1 solution and bond using custom made anodic bonding jig.

Chambers are monitored by Quartz "tuning fork" resonators (Figure 1b). One chamber (Fork 1) contains a heat exchanger to cool the ^{3}He. Fork 2 monitors the "isolated" chamber (Figure 1c,d). Pulses applied to Fork 2 heat the isolated chamber and heat flows through the micromachined channel. The relaxation following a heat pulse is measured. We have identified a thermal transport mechanism (thermomechanical heat flow) that is present only in the superfluid and then only when the mean free path is much longer than the height constraint. [5]

Measurements on supercooling of the A phase are in progress. The two phases (A and B) that are stable in the bulk are separated by a first order phase transition line. When the A phase is cooled below its stable region, it persists in a metastable state because nucleation of the B phase requires a significant energy cost. We observe supercooling and measure the width (in temperature) of the distribution of A to B nucleation events. We intend to map the pressure dependence of the supercooling and determine if supercooling is affected by the thermal channel which favors the A phase.

We have also examined the resonant frequency and quality factor of single layer graphene resonators both above (300-500 K) and below (80-300 K) room temperature (Figure 2). The critical point dryer was an essential tool in this fabrication. We find that the resonant frequency and quality factor increase as the temperature deviates from room temperature. The results are interpreted as evidence of the persistence of traces of polymer coatings used as part of the transfer process to deposit the single layer material from growth chamber to device. [3]

Former Physics Ph.D. students Nikolay Zhelev (now Corning Research), Roberto DeAlba (now NIST), and post-doctoral scientist Abhilash Sebastian (now Aalto University) fabricated these structures before they left Cornell. Results from these structures are now emerging or have been recently published.

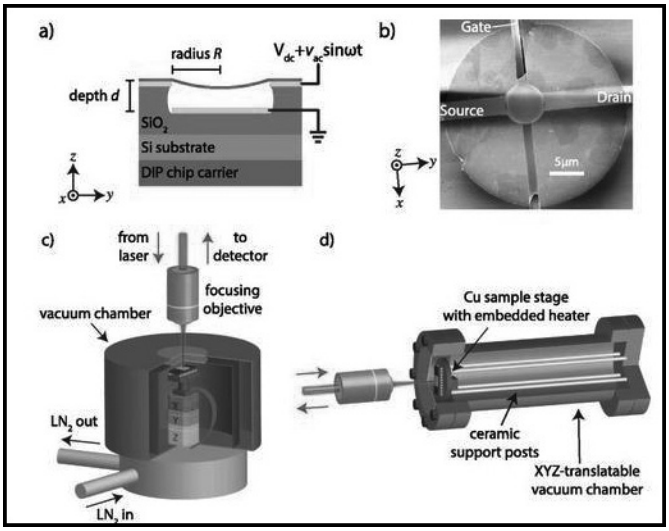

Figure 2: A. Cartoon cross-section of a graphene device. Suspended graphene (green) is pulled toward the back-gate via an applied voltage. B. False-color SEM image, showing the suspended graphene (green), metallic Source, Drain, and Gate (yellow), and surrounding SiO_2 substrate (grey). C. Liquid N_2 flow cryostat with optical access. Sample is mounted on a 24-pin Dual In-line Package (purple). D. Heated test chamber with optical window [3]. See full color version on pages xxviii-xxix.

References:

[1] Fabrication of microfluidic cavities using Si-to-glass anodic bonding, N. Zhelev, T. S. Abhilash, R. G. Bennett, E. N. Smith, B. Ilic, L. V. Levitin, X. Rojas, A. Casey, J. Saunders, and J. M. Parpia arXiv:1805.00958.

[2] The A-B transition in superfluid helium-3 under confinement in a thin slab geometry, N. Zhelev, T.S. Abhilash, E.N. Smith, R.G. Bennett, X. Rojas, L. Levitin, J. Saunders, and J.M. Parpia, Nature Comm. 15963 (2017).

[3] Temperature-dependence of stress and elasticity in wet-transferred graphene membranes, Roberto De Alba, T. S. Abhilash, Aaron Hui, Isaac R. Storch, Harold G. Craighead, and Jeevak M. Parpia, Journal of Applied Physics 123, 095109 (2018).

[4] Phase Diagram of the Topological Superfluid ^{3}He Confined in a Nanoscale Slab Geometry, L. V. Levitin, R. G. Bennett, A. Casey, B. Cowan, J. Saunders, D. Drung, Th. Schurig and J. M. Parpia, Science, 340 841-844, (2013).

[5] Thermal Conductivity of ^{3}He confined in a 1.1 μm sized channel, Jeevak Parpia, Anna Eyal, Nikolay Zhelev, Dmytro Lotnyk, Michael Terilli, Abhilash Sebastian, Eric Smith, http://meetings.aps.org/Meeting/MAR18/Session/A45.3.

Fabrication of Nanoscale Josephson Junctions for Quantum Coherent Superconducting Circuits

CNF Project Number: 1735-08

Principal Investigator: Britton L.T. Plourde

Users: Caleb Howington, Indrajeet, JJ Nelson

Affiliation: Department of Physics, Syracuse University

Primary Source of Research Funding: Army Research Office

Contact: bplourde@syr.edu, cjhowing@syr.edu, indraje@syr.edu, jjnelson@syr.edu

Website: http://plourdelab.syr.edu

Primary CNF Tools Used: ASML 300C DUV stepper, JEOL 9500, Plasma-Therm PT740

Abstract:

We fabricate nanoscale superconductor tunnel junctions and other structures for experiments involving quantum coherent circuits. Such circuits have shown great promise in recent years for explorations of quantum mechanics at the scale of circuits on a chip and for forming qubits, the foundational elements of a quantum computer. The quantum state of these superconducting qubits can be manipulated with microwave radiation at low temperatures. In addition, we are developing alternative techniques for probing the state of these qubits and controlling their quantum state, as well as superconducting metamaterial structures with novel microwave mode spectra for coupling to superconducting qubits.

Summary of Research:

The unique properties of nanoscale Josephson junctions enable a wide range of novel superconducting circuits for investigations in many diverse areas. In recent years, circuits composed of such junctions have emerged as promising candidates for the element of a quantum computer, due to the low intrinsic dissipation from the superconducting electrodes and the possibility of scaling to many such qubits on a chip [1]. The quantum coherent properties of the circuits are measured at temperatures below 50 mK with manipulation of the qubit state through microwave excitation.

We are currently working on a variety of experiments involving these nanoscale Josephson junctions and other superconducting structures that will allow us to probe novel quantum effects in our microwave circuits. We are fabricating superconducting circuits for forming low-temperature detectors of single microwave photons and for implementing a new scheme for the efficient readout of the quantum state of superconducting qubits [2-4]. We are also working with collaborators at the University of Wisconsin, Madison to develop hybrid quantum/classical superconducting chips that allow us to perform coherent quantum control of a superconducting qubit based on digital pulses from a Single Flux Quantum (SFQ) circuit [5,6].

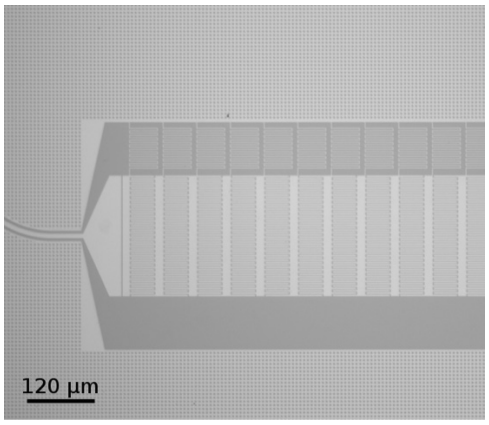

Figure 1: Optical micrograph of superconducting metamaterial transmission line resonator fabricated from Nb thin film on Si.

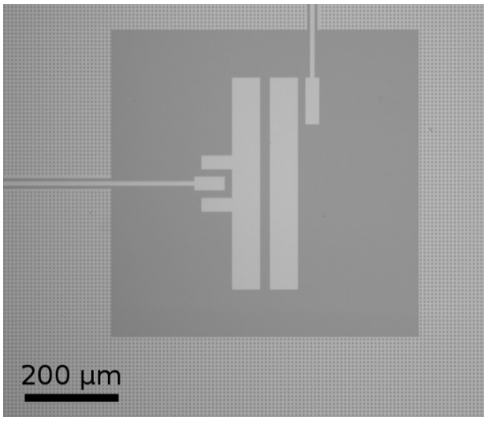

Figure 2: Optical micrograph of superconducting Nb qubit islands with coupling capacitor to metamaterial resonator.

In another effort, we are using particular combinations of superconducting lumped-circuit elements to engineer metamaterial transmission lines that exhibit novel mode structures characteristic of left-handed materials [7]. We are fabricating such metamaterial transmission lines from Al and Nb films on Si and characterizing these at low temperatures [8]. We are working on experiments to couple these left-handed lines to superconducting qubits for experiments involving the exchange of microwave photons [9].

We pattern these circuits at the CNF with nanoscale structures defined with electron-beam lithography on the JEOL 9500 integrated with photolithographically defined large-scale features. The junctions are fabricated using the standard double-angle shadow evaporation technique, in which a resist bilayer of copolymer and PMMA is used to produce a narrow PMMA airbridge suspended above the substrate. Evaporation of aluminum from two different angles with an oxidation step in between forms a small Al-AlO_x-Al tunnel junction from the deposition shadow of the airbridge. We have developed a process for defining these junctions with electron-beam lithography and we perform the aluminum evaporations in a dedicated chamber at Syracuse.

We pattern large-scale features using the ASML stepper, with electron-beam evaporation of Al, sputter-deposition of Nb, and PECVD deposition of SiO_2. Measurements of these circuits are performed in cryogenic systems at Syracuse University, including dilution refrigerators for achieving temperatures below 30 mK.

References:

[1] Clarke, J. and Wilhelm, F.K.; "Superconducting quantum bits"; Nature, 453, 1031 (2008).

[2] Govia, L.C.G., Pritchett, Emily J., Xu, Canran, Plourde, B. L. T., Vavilov, Maxim G., Wilhelm, Frank K., McDermott, R.; "High-fidelity qubit measurement with a microwave-photon counter"; Physical Review A 90, 062307 (2014).

[3] Howington, Caleb, Opremcak, Alex, Pechenezhskiy, Ivan, Vavilov, Maxim, McDermott, Robert, Plourde, Britton; "Cryogenic Digital Readout of Superconducting Qubits"; Bull. Am. Phys. Soc. 2018, http://meetings.aps.org/Meeting/MAR18/Session/B39.11.

[4] Opremcak, A, Pechenezhskiy, I., Howington, C., Christensen, B.G., Beck, M.A., Leonard Jr, E., Suttle, J., Wilen, C., Nesterov, K.N., Ribeill, G.J., Thorbeck, T., Schlenker, F., Vavilov, M.G., Plourde, B.L.T., McDermott, R.; "Measurement of a Superconducting Qubit with a Microwave Photon Counter"; arXiv:1803.01014 (2018).

[5] McDermott, R., Vavilov, M.; "Accurate Qubit Control with Single Flux Quantum Pulses"; Phys.Review Applied 2, 014007 (2014).

[6] Nelson, JJ, Leonard, E., Beck, M., Dodge, K., Howington, C., Ku, J., McDermott, R., Plourde, B. "Coherent Control of a Superconducting Transmon with Single Flux Quantum Pulses"; Bull. Am. Phys. Soc. 2018, http://meetings.aps.org/Meeting/MAR18/Session/L39.5.

[7] Egger, D.J. and Wilhelm, F.K.; "Multimode Circuit Quantum Electrodynamics with Hybrid Metamaterial Transmission Lines"; Physical Review Letters 111, 163601 (2013).

[8] Plourde, B.L.T., Wang, H., Rouxinol, F., LaHaye, M.D.; "Superconducting metamaterials and qubits"; SPIE 9500 Proceedings, Quantum Information and Computation XIII, 95000M (2015).

[9] Indrajeet, Sagar, Wang, H., Hutchings, M., LaHaye, M., Plourde, B., Taketani, B., Wilhelm, F.; "Multi-mode Circuit Quantum Electrodynamics with Superconducting Metamaterial Resonators"; Bull. Am. Phys. Soc. 2018, http://meetings.aps.org/Meeting/MAR18/Session/H33.9.

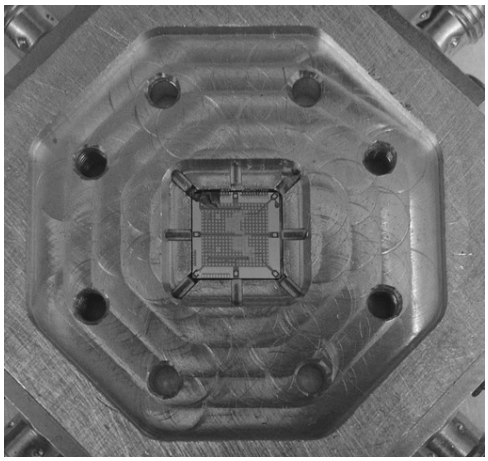

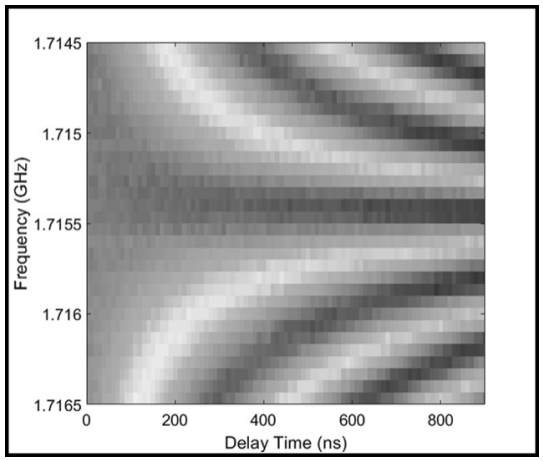

Figure 3, left: *Hybrid quantum/classical chip bonded into microwave package for implementation of qubit control with superconducting digital SFQ circuit.* ***Figure 4, right:*** *Coherent oscillation fringes of superconducting qubit driven with on-chip superconducting SFQ digital circuit.*

Fabrication of Superconducting Devices for Quantum Information Science

CNF Project Number: 1873-10

Principal Investigator: Britton L.T. Plourde

Users: Andrew Ballard, Jaseung Ku, Yebin Liu, Michael Senatore

Affiliation: Department of Physics, Syracuse University

Primary Source of Research Funding: Intelligence Advanced Research Projects Agency

Contact: bplourde@syr.edu, alballar@syr.edu, jku102@syr.edu, yliu166@syr.edu, masenato@syr.edu

Website: http://plourdelab.syr.edu

Primary CNF Tools Used: ASML 300C DUV stepper, JEOL 9500, Plasma-Therm PT740

Abstract:

We are fabricating nanoscale superconductor tunnel junctions and microwave resonators for investigations in quantum information science. Such circuits have shown great promise in recent years for forming qubits, the elements of a quantum computer. We are developing architectures involving multiple superconducting qubits and microwave resonators. This involves a combination of photolithographic processing and etching of large-scale features and electron-beam lithography for the tunnel junctions.

Summary of Research:

In recent years, circuits composed of nanoscale Josephson junctions have emerged as promising candidates for the foundational element of a quantum computer, due to the low intrinsic dissipation from the superconducting electrodes and the possibility of scaling to many such qubits on a chip [1]. The quantum coherent properties of the circuits are measured at temperatures below 50 mK with manipulation of the qubit state through microwave excitation.

We are working to develop architectures involving multiple superconducting qubits coupled to multiple low-loss microwave resonators [2-4]. We probe the coupling between each qubit and resonator by measuring the dispersive shift of the resonator frequency with the qubit detuned from the resonator. Some of our experiments are aimed at developing qubit designs that have reduced sensitivity to low-frequency magnetic flux noise that can lead to decoherence [2]. We are also investigating alternative qubit designs [3] that may lead to more efficient two-qubit gates for generating entanglement between circuits [4].

We pattern these circuits at the CNF with nanoscale structures defined with electron-beam lithography integrated with photolithographically defined large-scale features on Si and sapphire substrates. The junctions are fabricated using the standard double-angle shadow evaporation technique, in which a resist bilayer of copolymer and PMMA is used to produce a narrow PMMA airbridge suspended above the substrate.

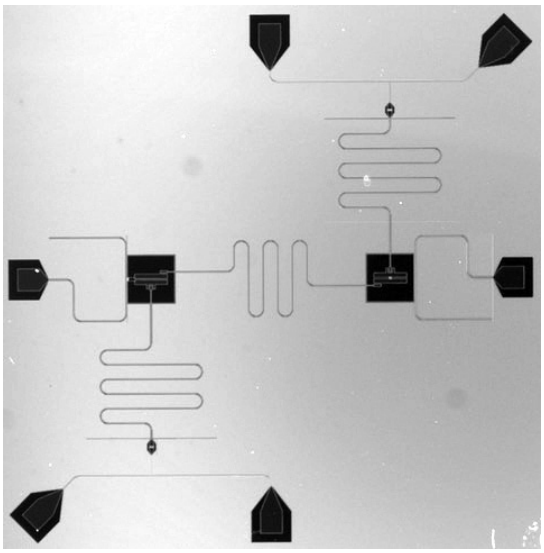

Figure 1: Optical micrograph of device with two superconducting qubits coupled by common microwave bus resonator with separate readout resonators for each qubit.

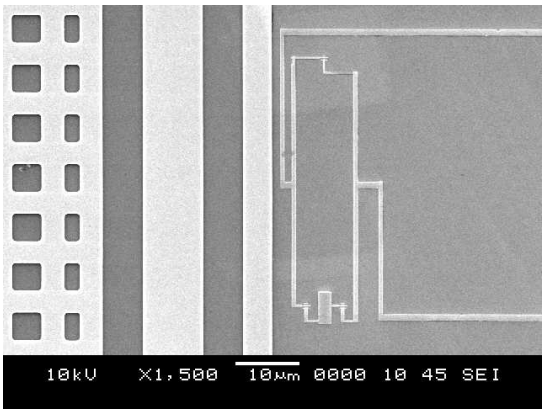

Figure 2: Scanning electron micrograph of superconducting loop with Josephson junctions for a capacitively shunted flux qubit.

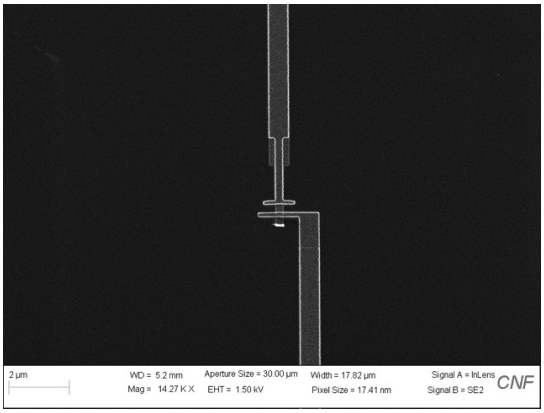

Figure 3: Scanning electron micrograph of cross-style Al-AlOx-Al Josephson junction for superconducting qubit patterned on the JEOL 9500.

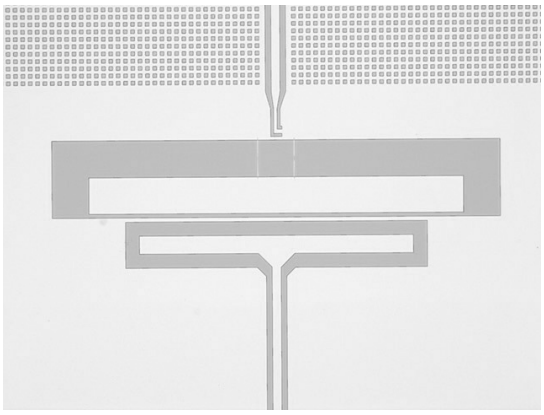

Figure 4: Optical micrograph of superconducting qubit for experiments probing the effects of magnetic flux noise on qubit decoherence.

Evaporation of aluminum from two different angles with an oxidation step in between forms a small Al-AlO_x-Al tunnel junction from the deposition shadow of the airbridge. We have developed a process for defining these junctions with electron-beam lithography on the JEOL 9500 and we perform the aluminum evaporations in a dedicated vacuum chamber at Syracuse. We pattern large-scale features using the ASML, with sputter deposition of superconducting Nb films in a dedicated vacuum system at Syracuse University. Microwave measurements of these circuits are performed in cryogenic systems at Syracuse University, including dilution refrigerators for achieving temperatures below 30 mK.

References:

[1] Clarke, J. and Wilhelm, F.K.; "Superconducting quantum bits"; Nature, 453, 1031 (2008).

[2] Hutchings, M. D. Hertzberg, Jared B., Liu, Y., Bronn, Nicholas T., Keefe, George A., Chow, Jerry M., Plourde, B.L.T.; "Tunable Superconducting Qubits with Flux-Independent Coherence"; Physical Review Applied 8, 044003 (2017).

[3] Ku, Jaseung, Liu, Yebin, Plourde, Britton, Hertzberg, Jared, Brink, Markus, Magesan, Chow, Jerry; "Capacitively Shunted Flux Qubits and Asymmetric Transmons for Multi-qubit Operations"; Bull. Am. Phys. Soc. 2018, http://meetings.aps.org/Meeting/MAR18/Session/L33.8.

[4] Corcoles, A. D., Gambetta, Jay M., Chow, Jerry M., Smolin, John A., Ware, Matthew, Strand, J. D., Plourde, B. L. T., Steffen, M.; "Process verification of two-qubit quantum gates by randomized benchmarking"; Physical Review A 87, 030301(R) (2013).

Anomalous Nernst Imaging of Uncompensated Moments in Antiferromagnetic FeRh Thin Films

CNF Project Number: 2091-11

Principal Investigator: Gregory D. Fuchs[1]

Users: Isaiah Gray[1], Gregory M. Stiehl[2]

Affiliations: 1. School of Applied and Engineering Physics, 2. Department of Physics; Cornell University, Ithaca, NY

Primary Source of Research Funding: Cornell Center for Materials Research from the National Science Foundation MRSEC Program, Grant No. DMR-1719875

Contact: gdf9@cornell.edu, ig246@cornell.edu, gms263@cornell.edu

Primary CNF Tools Used: GCA 5x stepper

Abstract:

We use anomalous Nernst microscopy to image uncompensated magnetic moments in Pt/FeRh <001> bilayers as a function of temperature and magnetic field. Uncompensated moments (UMs) in antiferromagnets (AFM) have been extensively studied in ferromagnetic (FM)/antiferromagnetic (AF) bilayers, where they are responsible for exchange bias, but their structure in a single antiferromagnetic layer is less well characterized. We image the emergence of the ferromagnetic phase in the 1st-order magnetic phase transition in FeRh. Below T_N we resolve μm-scale FM domains with large, spatially inhomogeneous vertical shifts to the $M(H)$ loop. This so-called vertical exchange bias signals the presence of bulk UMs with varying degrees of exchange-coupling to the local Néel order. Our measurements provide new insight into the structure of uncompensated moments within a single antiferromagnetic thin film.

Summary of Research:

In a simplified picture of a collinear Néel antiferromagnet, each spin is compensated by an oppositely-pointing spin on an adjacent lattice site, and therefore there is no net magnetic moment. In reality, uncompensated moments (UMs) form both in the bulk and at interfaces [1]. These UMs are of great practical importance because they are directly responsible for exchange bias in antiferromagnet /ferromagnet (FM) bilayers [2]; however, they are difficult to probe directly. In this work we use anomalous Nernst microscopy to image uncompensated moments in FeRh, which undergoes a 1st-order AFM/FM phase transition near T_N = 100°C [3] and therefore provides an ideal platform to study the interaction of ferromagnetism and antiferromagnetism in the same material.

We study 10 nm Pt/20 nm FeRh bilayers patterned into 3 μm × 30 μm Hall crosses. We first characterize the phase transition with anomalous Nernst imaging [4], shown in Figure 1. In agreement with previous imaging studies [5] we observe that FM domains first nucleate on defects and sample edges near 80°C, then percolate through the sample, and finally grow in size until the FM phase is uniform above 100°C.

At 25°C, we image μm-scale magnetic contrast, shown in Figure 2, which exhibits a ferromagnetic hysteresis loop averaged over the whole sample but unlike conventional FM samples does not saturate uniformly with field. Imaging at positive and negative field, we resolve signal from both unpinned domains, which switch with field, and pinned domains, which do not switch.

Plotting the average signal within adjacent ..m-scale pinned domains as a function of field in Figure 3, we obtain hysteretic $M(H)$ loops characteristic of a ferromagnet, but with unusual large vertical offsets signifying spatially inhomogeneous vertical exchange bias [6]. We explain these results in terms of bulk uncompensated moments exchange-coupled to the Néel order: large (> 1 μm) regions of UMs are strongly exchange-coupled and do not switch, while small (< 500 nm) regions of UMs are weakly exchange-coupled and can be reoriented with 1 kG field.

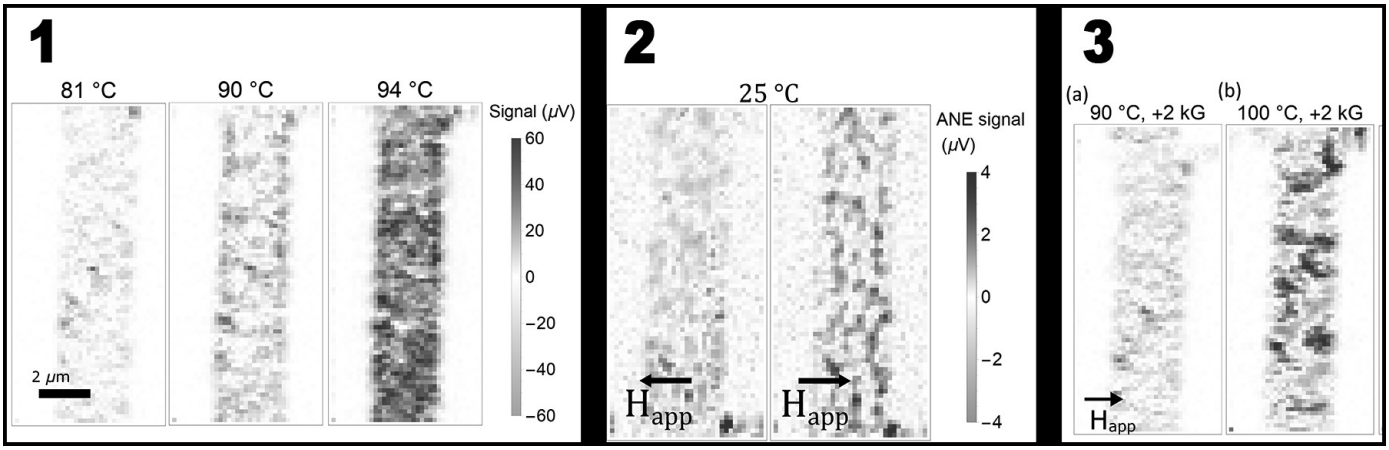

Figure 1, left: *Anomalous Nernst imaging of the 1st-order magnetic phase transition in FeRh. We observe the FM phase nucleating at sample edges and defects at 81°C, percolating through the sample at 90°C, and nearly uniform at 94°C.* ***Figure 2, middle:*** *Imaging FM contrast at 25°C, nominally in the antiferromagnetic phase, at positive and negative 1.3 kG field. The signal contains both unpinned FM domains, which reverse with field, and spatially inhomogeneous pinned domains, which do not reverse up to 5 kG field.* ***Figure 3, right:*** *Average signal from adjacent pinned domains as a function of field, yielding ferromagnetic* M(H) *loops with giant vertical shifts (vertical exchange bias). Pinned and unpinned domains correspond to strong and weak exchange-coupling between uncompensated moments and the bulk antiferromagnetic order.*

In conclusion, we image uncompensated moments in FeRh which exchange-couple to the bulk antiferromagnetic order in a complex, spatially inhomogeneous pattern. Our results establish anomalous Nernst microscopy as a powerful technique for imaging UMs in antiferromagnetic metals and provide insight into the interaction of coexisting AF and FM order in a single material.

References:

[1] J. Nogués and I. K. Schuller, J. Magn. Magn. Mater 192, 203-232 (1999).

[2] I. K. Schuller et al, J. Magn. Magn. Mater 416, 2-9 (2016).

[3] J. B. McKinnon et al, J. Phys. C: Solid State Phys. 3, S46 (1970).

[4] J. M. Bartell et al, Nat Comm. 6, 8640 (2015).

[5] C. Baldasseroni et al, Appl. Phys. Lett. 100, 262401 (2012).

[6] P.-H. Huang et al, Appl. Phys. Lett. 90, 062509 (2007).

Manipulating Topological Spin Textures in Spin-Valve Type Nanopillars

CNF Project Number: 2091-11

Principal Investigator: Gregory D. Fuchs

Users: Emrah Turgut, Isaiah Gray, Jason Bartell

Affiliation: Applied and Engineering Physics, Cornell University

Primary Source of Research Funding: Department of Energy

Contact: gdf9@cornell.edu, et329@cornell.edu

Primary CNF Tools Used: Heidelberg mask writer DWL 2000, GCA 5x stepper, JEOL e-beam lithography, even and odd evaporators, AJA ion mill, AJA sputtering, DISCO dicing saw

Abstract:

We study the properties of topological spin textures at nanoscale dimensions. We fabricate spin-valve nanopillars composed of a thin-film B_{20} FeGe below copper and $Ni_{80}Fe_{20}$ (permalloy) layers. Bypassing a current through these nanopillars, we explore magnetic field-dependent resistance to understand the non-trivial spin texture formed in the nanopillars, and at high current, manipulate the spin texture using spin-transfer torques. Our fabrication and characterization study of these structures is aimed at realizing future power-efficient memory devices.

Summary of Research:

Transition metal germanides (TMGs) have a non-centrosymmetric crystal structure, which creates a non-vanishing asymmetric exchange energy in addition to the common symmetric exchange in ferromagnets [1-3]. In an external magnetic field, asymmetric exchange can stabilize chiral and topological spin textures, including magnetic skyrmions and helices. These spin textures are functionally a magnetic quasi-particle in which information can be stored and manipulated with a very low energy as compared to other magnetic storage modalities.

The potential application in energy-efficient storage and logic applications makes understanding the nanoscale spin dynamics in these TMGs crucial. Studying their nanoscale spin dynamics requires the fabrication of spin valve nanopillars made of TMGs, transition metals, and ferromagnetic multilayers and with a characteristic diameter of 100 nm. The nanoscale diameter is necessary to creating large current densities and is promising for high-density magnetic storage applications. A schematic cartoon of a nanopillar is shown in Figure 1. The TMG is iron germanium (FeGe) in this case.

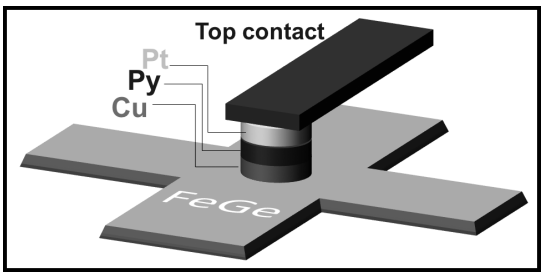

Figure 1: A cartoon picture of the nanopillar. The bottom FeGe layer is a chiral magnet that can stabilize magnetic skyrmions. The permalloy layer is a well-understood ferromagnetic layer that can generate spin current when a charge current passes through the nanopillar. The Cu layer works as spin-transport layer while decoupling the magnetic moments of permalloy and FeGe.

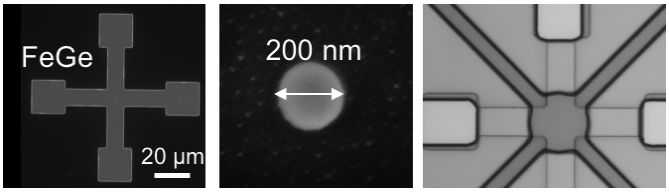

Figure 2: Micrographs of some of the steps during the nanopillar fabrication. The left and middle SEM micrographs are the bottom FeGe layer and a 200-nm-diameter pillar. The right optical micrograph is the final contact pads before deposition.

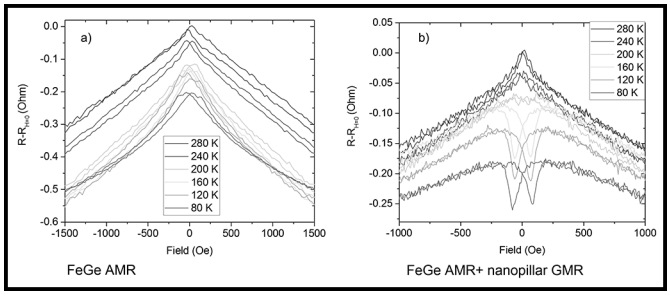

Figure 3: Magnetoresistance measurements of a nanopillar at varied temperatures. a) shows the resistance of the bottom FeGe layer only, which is a typical AMR that is less sensitive to the sample temperature. The right graph b), however, shows the combination of the FeGe AMR and the nanopillar GMR, which shows strong temperature dependence.

We grow FeGe on a Si <111> substrate with MBE before transferring the wafer into a sputtering system where we deposit copper, permalloy, and platinum layers under ultrahigh vacuum. Then, we fabricate magnetic nanopillars devices with multiple optical and electron-beam lithography steps, some of which are shown in Figure 2. The left and the middle images are scanning electron micrographs of the bottom FeGe layer and a 200-nm-diameter pillar, respectively. The right image is an optical micrograph of the final contact-pads before their deposition.

Our structure has complicated spin configurations due to the chiral magnetism of the FeGe layer. We study the magnetoresistance (MR) properties of the nanopillars to understand their equilibrium magnetization configurations. For example, FeGe has temperature-and field-dependent phases, including paramagnetic, spin-helix, magnetic skyrmion, and field polarized states. Moreover, the permalloy layer can stabilize magnetic vortices and multi-domain magnetic textures. By making such nanopillars, we enable interactions between these magnetic textures. We vary the sample temperature and magnetic field orientation as we measure the resistance of the nanopillar, which should reflect the magnetic configuration of the individual nanopillar.

In Figure 3, we show field-dependent MR curves at different temperatures. The left graph, Figure 3a, shows the anisotropic MR (AMR) of the bottom FeGe layer, which is isolated by measuring between bottom contacts. We observe a slight change of anisotropic MR as a function of temperature. On the other hand, Figure 3b shows both the AMR of FeGe and the giant MR (GMR) of the pillar, which is measured between the nanopillar top and bottom contacts. At high temperatures (the purple curve), FeGe is in the paramagnetic phase; therefore, we do not observe a GMR response of the FeGe/permalloy spin valve. However, at low temperatures (the red and orange curves), the GMR response is strong. As the permalloy layer switches at around 100 Oe, the total MR varies substantially.

Our experiment shows an interesting but non-trivial magnetoresistance behavior. To understanding it better, our next effort will be micromagnetic modeling.

In summary, we fabricate spin valve nanopillars and study their MR to understand topological spin textures in confined geometries. Our preliminary measurements show a strong GMR effect. Further modeling will shed light on these complicated spin configurations.

References:

[1] Nagaosa, et al., Nature Nanotechnology 8, 899 (2013).

[2] Turgut, et al., Physical Review B 95, 134416 (2017).

[3] Turgut, et al., Journal of Applied Physics 122, 183902 (2017).

Diamond-Based Hybrid Quantum Mechanical Systems

CNF Project Number: 2126-12

Principal Investigator: Gregory D. Fuchs[1]

Users: Huiyao Chen[2], Evan R. Macquarrie[2]

Affiliations: 1. School of Applied and Engineering Physics, 2. Department of Physics; Cornell University

Primary Source of Research Funding: Office of Naval Research (Grants No. N000141410812 and No. N000141712290)

Contact: gdf9@cornell.edu, hc846@cornell.edu

Website: http://fuchs.research.engineering.cornell.edu

Primary CNF Tools Used: GCA 5x stepper, Heidelberg mask writer DWL2000, AJA sputtering deposition system, YES Asher, P10 profilometer, Westbond 7400A ultrasonic wire bonder

Abstract:

Nitrogen vacancy (NV) centers are atom-like quantum emitters in diamond, with narrow orbital transition linewidth and a long-lived spin coherence that persists to room temperature. Diamond-based microelectromechanical systems (MEMS) devices integrate these quantum defects with classical mechanics, providing direct coupling between diamond NV center spin/orbital states and phonons in a mechanical resonator. We demonstrate orbital state manipulation of a single NV center with a GHz diamond high-overtone bulk acoustic resonator (HBAR). Furthermore, we are developing a new diamond MEMS device that is designed to realize the control of mechanical quantum states using diamond spins, which is potentially useful for quantum-enhanced metrology and quantum information processing.

Summary of Research:

Diamond-based hybrid quantum spin-mechanical systems marry the two fields of microelectromechanical systems (MEMS) and quantum information science with the goal of realizing coherent mechanical control of diamond nitrogen-vacancy (NV) centers [1] and quantum enhanced mechanical sensing [2]. Following the recent demonstration of coherent mechanical control of spin state of NV centers [3,4], we recently demonstrated orbital state manipulation of a single NV center using a diamond MEMS device [5].

The device adopts the design of a high-overtone bulk acoustic resonator (HBAR) device fabricated from a diamond substrate using a zinc oxide (ZnO) piezoelectric mechanical transducer. We study the resonant optical orbital transition of a single NV center under the influence of coherent phonon driving from a mechanical resonator (Figure 1). We demonstrated coherent Raman sidebands out to the ninth order and orbital-phonon interactions that mix the two excited-state orbital branches. These interactions are spectroscopically revealed through a multi-phonon Rabi splitting of the orbital branches, which scales as a function of resonator driving amplitude.

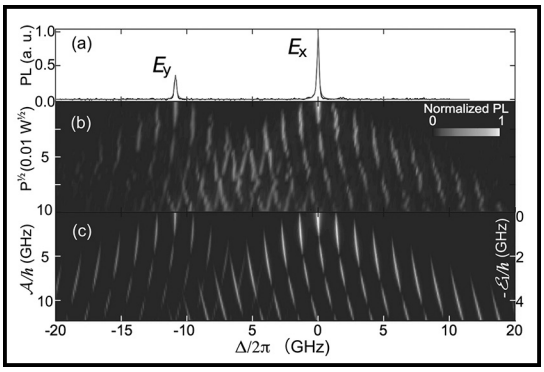

Figure 1: (a) Photoluminescence (PLE) spectrum of a NV center with orbital E*-state splitting of 10.6 GHz in the absence of mechanical driving. (b) Phonon-dressed state PLE measurement with mechanical driving at 1.3844 GHz. The mechanical driving amplitude is proportional to square root of the power applied to the transducer,* $P^{1/2}$*. Sideband transitions and level repulsion are evident in between* E *states. (c) Reconstruction of experimental data through quantum master equation simulation.*

We show that the application of mechanical driving to engineering NV center orbital states can potentially stabilize NV center optical transition by reducing its sensitivity to fluctuating parasitic electric fields.

For quantum-enhanced mechanical sensing, the physical interaction, NV center electron spin-phonon coupling is rather weak in the current device design, which limits their application to quantum acoustodynamics (QAD) [6]. Engineering new generation of diamond MEMS device with higher quality factors, smaller mode volumes and higher NV-center density can help increase the coupling rate, and potentially enable sensing and control of resonator mechanical state using NV centers. We are in the process of developing the next generation device (Figure 2), a parabolic diamond HBAR. The device consists a 10 μm thick diamond membrane as the substrate, fabricated through deep reactive ion etching from a 100 μm thick diamond chip. On the etched surface, we mill a parabolic solid immersion lens (SIL) using focused ion beam (Figure 3). The parabolic SIL serves two purposes: 1) create a stable plano-convex acoustic cavity to confine the active phonon mode; 2) improve light collection efficiency from NV centers in the SIL by eliminating surface refraction.

Finally, we fabricate a piezoelectric transducer (Figure 4) using photolithography and DC sputtering, whose size mode-matches with the confined acoustic beam. The device is proposed to have frequency and quality-factor product $fQ > 10^{13}$, enabling defect-assisted quantum mechanical sensing.

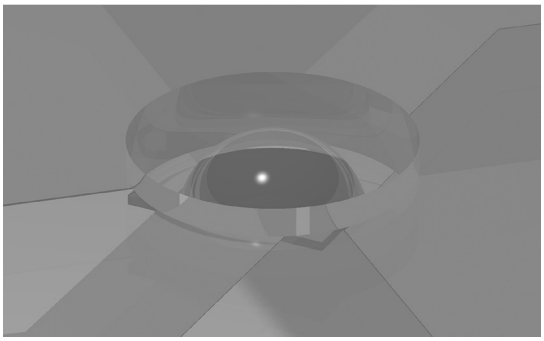

Figure 2: 3D illustration of the next generation device, with integrated plano-convex diamond acoustic cavity and mechanical transducer.

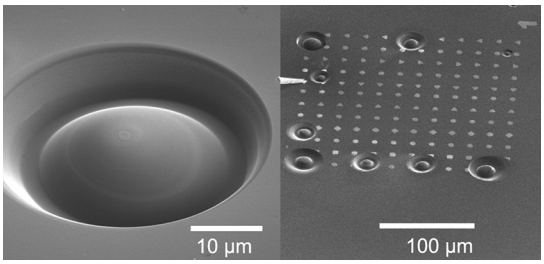

Figure 3: SEM images of solid immersion lenses on diamond milled through focused ion beam.

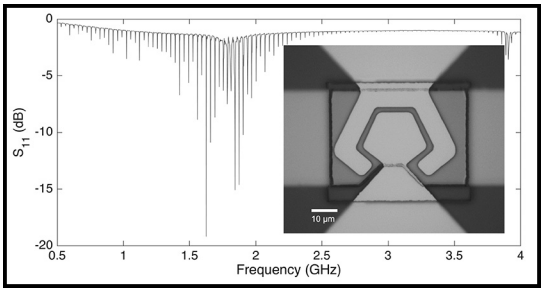

Figure 4: Electromechanical response of a HBAR sample measured by vector network analyzer. The inset shows an optical image of a device.

References:

[1] Lee, D., et al. Topical Review: Spins and mechanics in diamond. J. Opt. 19 033001 (2017).

[2] Barson, M. S.J., et al. Nanomechanical Sensing Using Spins in Diamond. Nano Lett. 17 (3), 1496-1503 (2017).

[3] MacQuarrie, E. R., et al. Mechanical Spin Control of Nitrogen-Vacancy Centers in Diamond. Phys. Rev. Lett. 111, 227602 (2013).

[4] Barfuss, A., et al. Strong mechanical driving of a single electron spin. Nat. Phys. 11, 820-824 (2015).

[5] Chen, H. Y., et al. Orbital state manipulation of a diamond nitrogen-vacancy center using a mechanical resonator. Phys. Rev. Lett. 120,167401 (2018).

[6] Chu, Y. W., et al. Quantum acoustics with superconducting qubits. Science, 358, 6360, 199-202 (2017).

Properties of Isolated Defects in Hexagonal Boron Nitride

CNF Project Number: 2126-12

Principal Investigator: Gregory D. Fuchs

Users: Nicholas R. Jungwirth, Nikhil Mathur, Raphael Daveau

Affiliation: Applied and Engineering Physics, Cornell University

Primary Source of Research Funding: National Science Foundation

Contact: gdf9@cornell.edu, nrj32@cornell.edu, nm648@cornell.edu, rsd228@cornell.edu

Website: http://fuchs.research.engineering.cornell.edu

Primary CNF Tools Used: Scanning electron microscope, contact aligner, profilometer

Abstract:

We investigate the optical properties of defect-based single photon sources in hexagonal boron nitride (hBN) produced via solvent exfoliation (S-hBN) and mechanical exfoliation (M-hBN). Single defects found in S-hBN exhibit spectrally narrow zero-phonon emission and an absorption and emission dipole that may or may not be aligned parallel to one another. Defects found in wide area (> 50 × 50 μm) M-hBN multilayer flakes possess a broader zero phonon line and are less bright than the defects in S-hBN flakes. To study M-hBN, we develop a reliable method for mechanically exfoliating bulk h-BN crystals and precisely transferring it to a Si/SiO_2 substrate. Optically stable defects are subsequently created in the flake via an argon plasma etch combined with a thermal annealing treatment. The investigated defects may be in regions of the flake that is in contact with the substrate or, alternatively, in regions that are suspended over pre-patterned holes. Defects in the suspended region are not influenced by the substrate and may potentially couple to the mechanical modes of the resulting hBN drumhead.

Summary of Research:

Point defects in wide bandgap semiconductors exhibit quantum emission and have been identified as candidates for applications in quantum optics, precision sensing, and quantum information technologies [1]. Defects have been optically isolated in three-dimensional materials such as diamond, SiC, ZnO, and GaN, and more recently in two-dimensional materials such as transition metal dichalcogenides (TMDs) and hexagonal boron nitride (hBN) [2-6]. The defects in hBN exhibit ultrabright and polarized single photon emission. However, these single photon sources also exhibit significant defect-to-defect variation, making the comparison of experimental results with theoretical predictions difficult. In this work we compare the optical properties of single photon sources in hBN samples produced via solvent exfoliation (S-hBN) and mechanical exfoliation (M-hBN).

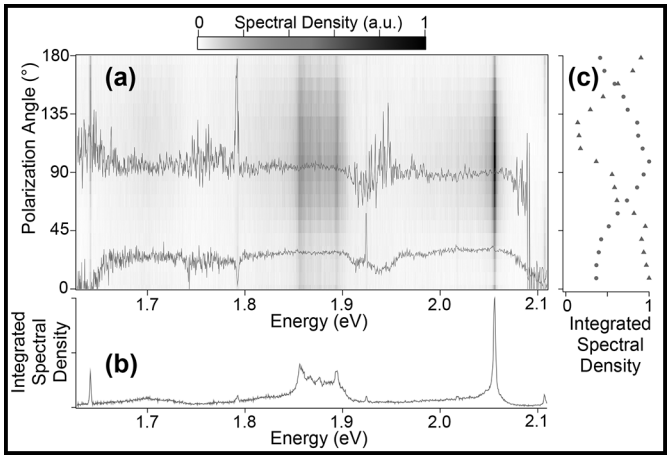

Figure 1: Spectrally resolved polarization measurements of an isolated defect in S-hBN revealing that the absorption and emission dipoles are misaligned.

Figure 1 shows a set of spectrally resolved polarization measurements made on a single defect in S-hBN. Figure 1a is a two-dimensional image plot revealing the fluorescence intensity of light emitted at a particular polarization angle. It was obtained by rotating a polarization analyzer in the collection path and collecting an emission spectrum at each orientation of the polarization analyzer. By vertically integrating the columns in the plot, we recover the unpolarized emission spectrum, shown in Figure 1b. In the unpolarized emission spectrum, a narrow zero phonon line (ZPL) and phonon sideband (PSB) are evident at ~ 2.05 eV and ~ 1.88 eV, respectively. By horizontally integrating the

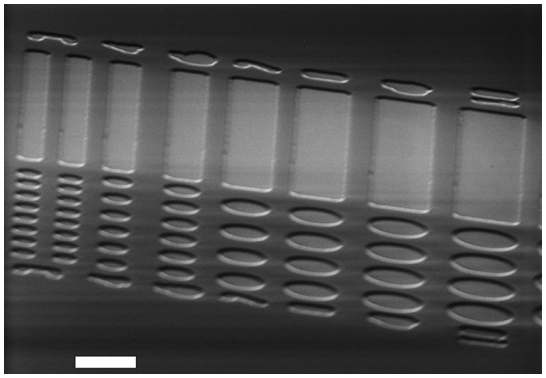

Figure 2: Scanning electron microscope image of holes and trenches fabricated onto a Si/SiO_2 substrate. The scale bar is 10 μm.

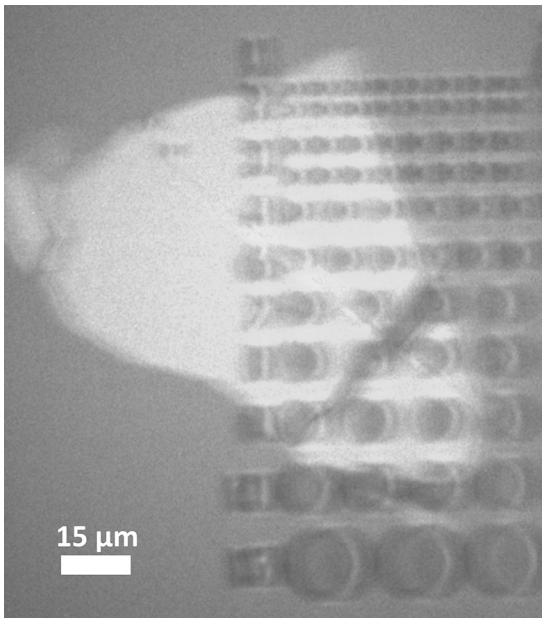

Figure 3: Optical microscope image of an hBN flake transferred to a region of the substrate containing holes and trenches.

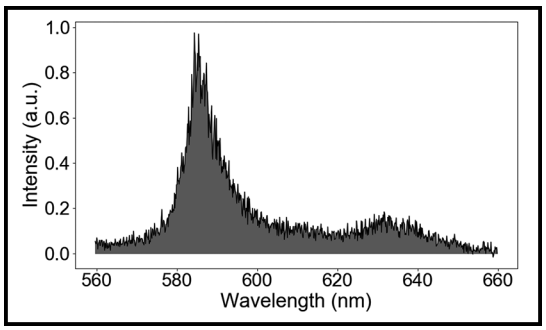

Figure 4: Emission spectrum of a single defect in M-hBN.

rows in Figure 1a we recover the spectrally averaged emission polarization profile (circles, Figure 1c). For comparison, the spectrally averaged excitation polarization profile is included as well (triangles, Figure 1c). Note that the absorption and emission dipoles are misaligned. This is confirmed by the spectrally resolved orientation of the emission and absorption dipoles, shown as the upper and lower traces, respectively, in Figure 1a.

To investigate defects in M-hBN, we developed a process of mechanically exfoliating bulk hBN crystals and precisely transferring them onto pre-patterned Si/SiO_2 substrates. Figure 2 is a scanning electron microscopy image of one such pre-patterned substrates revealing holes and trenches. Large area ($> 50 \times 50$ μm) M-hBN flakes may then be suspended over these holes (Figure 3). As-transferred M-hBN exhibits very low defect density, making it difficult to optically isolate individual defects. To increase the defect density, we argon etch as-transferred flakes and subsequently anneal the samples in nitrogen at 850°C for 30 minutes. After this sample treatment the defect density is enhanced and individual emitters maybe studied in suspended regions and in supported regions. Defects studied in suspended regions are not influenced by the substrate whereas defects in the supported regions may be influenced by charge traps in the underlying substrate.

Figure 4 is a room-temperature emission spectrum of a single defect in a suspended region of the M-hBN shown in Figure 3. Note that similar to S-hBN defects, this M-hBN defect also exhibits a broad ZPL and a PSB that is red-shifted from the ZPL by ~ 165 meV.

References:

[1] J. R. Weber, W. F. Koehl, J. B. Varley, A. Janotti, B. B. Buckley, C. G. Van de Walle, and D. D.Awschalom, Proc. Natl. Acad. Sci. 107, 8513 (2010).

[2] N. R. Jungwirth, Y. Y. Pai, H. S. Chang, E. R. MacQuarrie, K. X. Nguyen, and G. D. Fuchs, J. Appl.Phys. 116, 043509 (2014).

[3] N. R. Jungwirth, H.-S. Chang, M. Jiang, and G. D. Fuchs, ACS Nano 10, 1210 (2016).

[4] T. T. Tran, K. Bray, M. J. Ford, M. Toth, and I. Aharonovich, Nat. Nanotechnol. 11, 37 (2015).

[5] N. R. Jungwirth, B. Calderon, Y. Ji, M. G. Spencer, M. E. Flatté, and G. D. Fuchs, Nano Lett. 16,6052 (2016).

[6] N. R. Jungwirth and G. D. Fuchs, Phys. Rev. Lett. 119, (2017).

Extreme Light-Bending and Trapping with a Simple Cubic Optical Photonic Crystal

CNF Project Number: 2173-12

Principal Investigator: Shawn-Yu Lin

Users: Brian Frey, Alex Kaiser

Affiliation: Department of Physics, Rensselaer Polytechnic Institute, Troy, NY 12180

Primary Source of Research Funding: United States Department of Energy, Office of Science, Basic Energy Sciences

Contact: sylin@rpi.edu, freyb3@rpi.edu, kaisea2@rpi.edu

Primary CNF Tools Used: PVD75 sputter deposition, AJA sputter deposition, ASML deep-ultraviolet stepper, Oxford reactive-ion-etcher, Trion inductively-coupled plasma etcher, GSI PECVD tool, Orbis chemical-mechanical polisher, Zeiss scanning electron microscope, Veeco atomic force microscope, CVC electron-beam evaporator

Abstract:

A sub-micron TiO_2 simple cubic photonic crystal with lattice constant 450 nm was fabricated and used to characterize a newly-discovered light-bending mechanism wherein the Poynting vector lies nearly parallel to the photonic crystal interface. Absorption enhancement approaching 100 times was observed compared to a reference TiO_2 film. Several enhancement peaks in the region from 600-950 nm wavelength far exceed both the ergodic and square surface-grating light-trapping limits. These results can be applied to any future light trapping applications such as phosphor-converted white light generation, water-splitting, or thin-film solar cells, where increased response in areas of weak absorption is desired.

Summary of Research:

In several areas of opto-electronics, the efficient conversion of light into useful energy is paramount. Typically, performance is limited by different factors, such as weak near-infrared absorption (crystalline silicon [1]), or charge diffusion length (amorphous silicon [2]). To circumvent these limitations while addressing cost [3], and efficiency concerns [4], it is beneficial to engineer structures that can alter the optical-path-length through these devices without using more material. This is referred to as "light trapping" [5].

In this research, we identify a precise light-trapping mechanism, which is due to photonic crystal (PC) refraction. This effect, called parallel-to-interface refraction (PIR), extends the path-length by orders of magnitude by coupling light into modes for which the Poynting vector lies nearly parallel to the PC interface [5,6]. Accordingly, we have constructed a simple cubic PC from weakly-absorbing TiO_2 to demonstrate orders-of-magnitude enhancement over a reference TiO_2 film. The conclusions that follow are general and not restricted to any material.

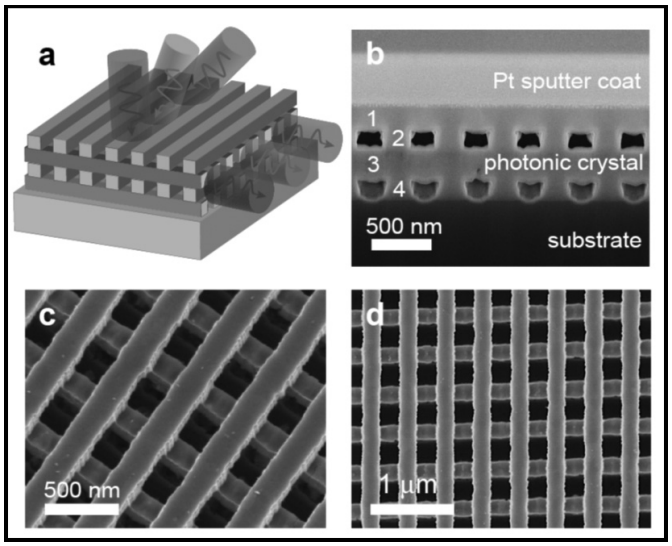

Figure 1: Schematic of a TiO_2 simple cubic photonic crystal. (a) Schematic of TiO_2 PC depicting parallel-to-interface refraction. (b) Cross-section side view, (c) perspective view, and (d) top-view pictures of fabricated TiO_2 PC.

The structure used for this study, depicted in Figure 1.a, is a stacked, 4-layer TiO_2 simple cubic PC [7]. It was fabricated with photolithography and etch steps in a layer-by-layer process using the ASML deep-ultraviolet stepper and Oxford reactive ion etcher. A complete description of the fabrication process is described elsewhere [8], but the results are summarized in Figure 1.

To investigate PIR, we measured the absorption of our PC, which is plotted in Figure 2. The absorption of a

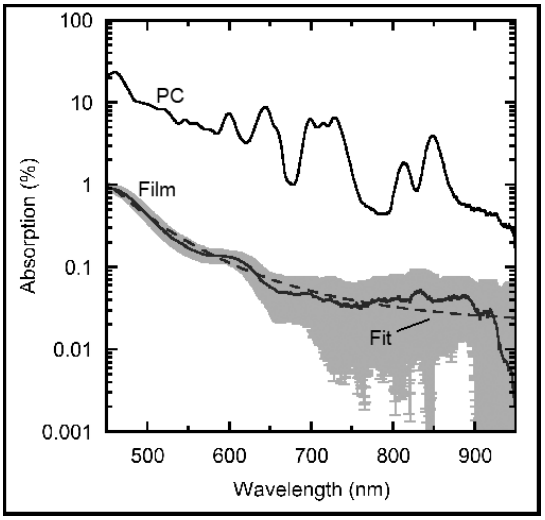

Figure 2: Absorption spectra for PC and reference film.

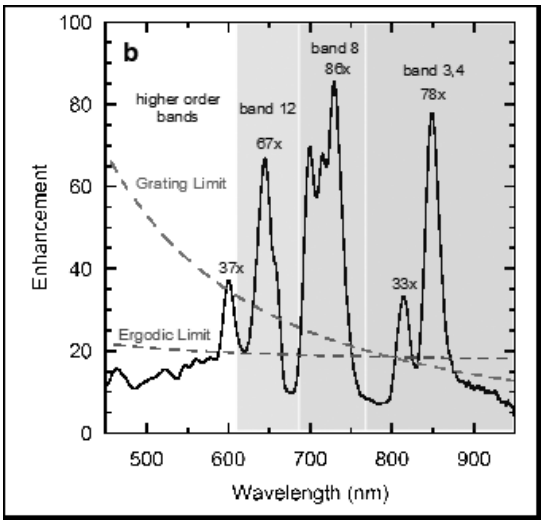

Figure 3: Absorption enhancement for PC. Also shown are the lines for the ergodic limit and 2D grating limit.

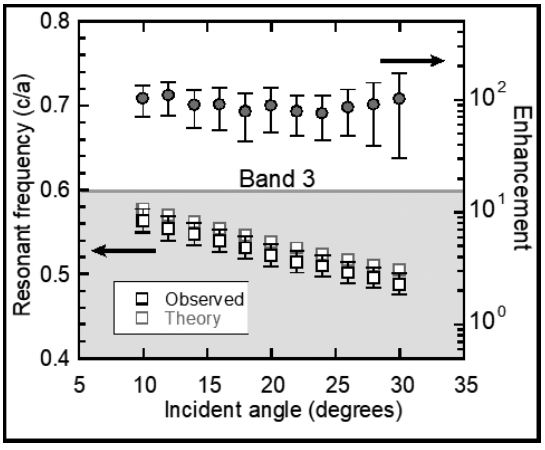

Figure 4: Absorption peak frequency and peak enhancement vs. incident angle for band 3. Filled circles are measured enhancement at the peak frequency. The bounded box shows the frequency range for band 3.

reference TiO_2 planar film of comparable thickness is also shown for comparison. Figure 2 shows that the film absorption below the bandgap is less than 1% and decays exponentially. Notably, in the range from 600-800 nm, the PC shows a series of absorption peaks that approach 10%, while the film absorption is < 0.1%. Also, a pair of peaks observed for the PC between 800-900 nm with max values of ~ 2-4%; here the film shows ~ 0.03% absorption.

In Figure 3, the enhancement factor η, defined as the ratio of the PC and film absorption values, is plotted as a function of wavelength. Here, the doublet of peaks observed at longer wavelengths corresponds to η ~ 30 and 80 times, respectively. The maximum enhancement for peaks in the mid-wavelength region is close to 100 times. These peaks also surpass, by multiple times, two theoretical limits also shown for comparison: one is the ergodic limit of $4n^2$ [9], and the other is based on a square surface-grating architecture [10]. To show that this is attributable to PIR, the angular dependence of the resonant frequencies for the band 3 absorption peaks is shown in Figure 4. The data not only agree well with the predicted PIR frequencies from theory, but there is a one-to-one correspondence between theory and observation and the scaling of the resonant frequency with θ_0 is virtually identical. Furthermore, the peak enhancement is approximately angle-independent at η ~ 100 times. The data experimentally validate PIR and provide direct proof of its contribution to absorption enhancement in a simple cubic PC.

PIR provides an opportunity to use simple cubic PCs as an ordered, three-dimensional network that refracts light according to the dispersion relation. This approach to absorption enhancement is amenable to infiltration by various agents, such as dyes, polymers, and nanophosphors, and is also suitable for investigating PC-induced light emission enhancement. We anticipate that the scope of these results will extend beyond thin-film solar cells to other applications, like phosphor conversion in light-emitting diodes, and water-splitting.

References:

[1] Redfield, D. Multiple-pass thin-film silicon solar cell. Appl. Phys. Lett. 25, 647-648 (1974).

[2] Carlson, D. E., and Wronski, C. R. Amorphous silicon solar cell. Appl. Phys. Lett. 28, 671-673 (1976).

[3] Shah, A., Torres, P., Tscharner, R., Wyrsch, N., and Keppner, H. Photovoltaic technology: the case for thin-film solar cells. Science 285, 692-698 (1999).

[4] Vetterl, O., et al. Thickness dependence of microcrystalline silicon solar cell properties. Sol. Energ. Mat. Sol. 66, 345-351 (2001).

[5] Chutinan, A., and John, S. Light trapping and absorption optimization in certain thin-film photonic crystal architectures. Phys. Rev. A 78, 023825 (2008).

[6] Kuang, P., Deinega, A., Hsieh, M. L., John, S., and Lin, S. Y. Light trapping and near unity solar absorption in a three-dimensional photonic-crystal. Opt. Lett. 38, 4200-4203 (2013).

[7] Frey, B. J., et al. Effectively infinite optical pathlength created using a simple cubic photonic crystal for extreme light trapping. Sci. Rep. 7, 4171 (2017).

[8] Frey, B. J., Kuang, P., Lin, S. Y., Jiang, J. H., and John, S. Large area fabrication of a simple cubic metal-oxide photonic crystal for light trapping applications. J. Vac. Sci. Technol. B 33, 021804 (2015).

[9] Yablonovitch, E. Statistical ray optics. J. Opt. Soc. Am. 72, 899-907 (1982).

[10] Yu, Z., Raman, A., and Fan, S. Fundamental limit of light trapping in grating structures. Opt. Express 18, A366-A380 (2010).

Development of Scanning Graphene Hall Probes for Magnetic Microscopy

CNF Project Number: 2361-15

Principal Investigator: Katja C. Nowack

User: Brian T. Schaefer

Affiliations: Laboratory of Atomic and Solid-State Physics, Department of Physics; Cornell University

Primary Sources of Research Funding: Cornell Center for Materials Research with funding from the NSF MRSEC program (DMR-1719875), National Science Foundation Graduate Research Fellowship under Grant No. DGE-1650441

Contact: kcn34@cornell.edu, bts72@cornell.edu

Website: http://nowack.lassp.cornell.edu/

Primary CNF Tools Used: Veeco Icon AFM, Zeiss Supra SEM/Nabity, odd-hour evaporator, even-hour evaporator, Trion etcher, 5x stepper, Oxford 100 etcher, Plasma-Therm Versaline

Abstract:

We discuss our progress on developing scanning Hall probes using graphene as the sensitive material, with the goal to perform magnetic imaging experiments with submicron resolution. Our devices demonstrate a promising Hall sensitivity at cryogenic temperatures competitive with that of commercially available Hall probes. We plan to include a deep etch surrounding the sensitive area of the device to facilitate alignment and scanning over samples.

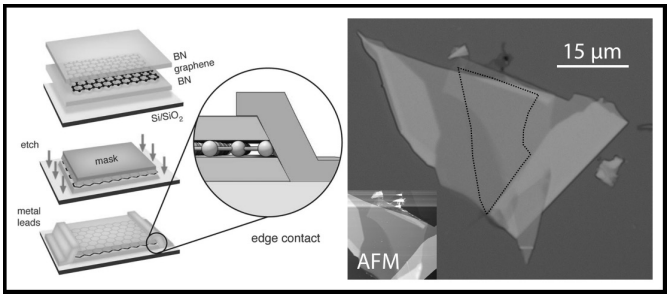

Figure 1: Left panel: overview of process from [3], used with permission. Right panel: a monolayer graphene flake (dotted outline) sandwiched between flakes of hexagonal boron nitride. Inset: AFM image, scaled down.

Summary of Research:

Scanning magnetic probe microscopy is a useful technique to study magnetism and electronic transport in materials because it provides a direct spatial map of the magnetic landscape above the sample surface. We currently use superconducting quantum interference device (SQUID) magnetometers for our imaging experiments, but these probes only operate at low temperatures and magnetic fields under ~ 1 Tesla [1]. In contrast, scanning Hall probes permit imaging in a strong magnetic field, over a much larger temperature range, and with potentially higher spatial resolution than SQUIDs [2]. To compete with the field sensitivity of a SQUID and to enable local fabrication, we choose to fabricate Hall probes from graphene encapsulated in hexagonal boron nitride (hBN) with one-dimensional edge contacts (Figure 1). Devices made with this architecture possess a remarkably low level of disorder, permitting tunability to low carrier density (~ 10^{10} cm^{-2}) to maximize the Hall response while maintaining a high mobility that enables low-noise measurements [3].

Our process is derived from the steps described in Ref. [3], with the important modification to include an aligned top gate in the design (Figure 2, inset), which shields the graphene layer from electrostatic inhomogeneity on the sample. We exfoliate graphene and hBN onto silicon chips and select monolayer flakes of graphene and uniform flakes of hBN using optical and atomic-force microscopy (Veeco AFM). Using the van der Waals assembly technique [3,4], we use a polymer stamp to sequentially pick up and stack a hBN/graphene/hBN heterostructure (Figure 1). We then release the stack onto a heavily doped SiO_2/Si substrate pre-patterned with alignment marks and metal contacts, dissolve the polymer in chloroform for several hours, and anneal in high vacuum at 350°C for three hours.

We again use AFM to identify regions of the stack that are flat and free of bubbles or wrinkles, and then use electron-beam lithography (Nabity) to define a metal (Cr/Au/Pt) top gate in a Hall bar or Hall cross geometry. In a second lithography step, we pattern an etch mask, leaving the edges of the top gate exposed to translate the shape of the topgate directly into the stack. We use an

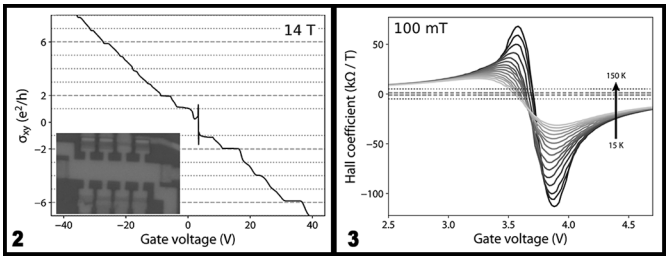

Figure 2, left: *Dependence of the Hall conductance on carrier density in a large external magnetic field. The dashed lines indicate expected conductance plateaus for degenerate spin and valley Landau levels, while the dotted lines indicate the conductance plateaus for lifted spin-valley degeneracy. Inset: optical image of the device.* ***Figure 3, right:*** *Hall coefficient (sensitivity) of the device from Figure 2 measured at 100 mT and at temperatures from 15 K (dark) to 150 K (light). The light dashed line marks a typical Hall coefficient for GaAs-based Hall probes [8], and the dark dotted line marks the maximum Hall coefficient previously reported for graphene devices at room temperature [7].*

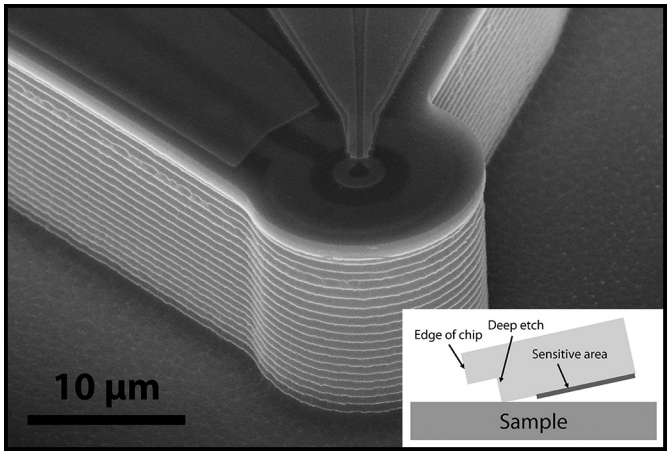

Figure 4: Deep etch surrounding the pickup loop of a SQUID magnetometer.

inductively coupled plasma of CHF_3, O_2, and Ar (Trion etcher) to selectively etch hBN, creating a step-like edge profile exposing a few-nm-wide strip of graphene [5]. In a final electron-beam lithography step, we pattern, deposit, and lift off Cr/Au/Pt contacts overlapping the exposed graphene edge. To protect the devices from mechanical stresses during scanning, we evaporate an ~ 80 nm layer of SiO_2 over the completed device.

We characterize device quality by measuring Hall voltage as a function of back gate voltage in an applied magnetic field. In a large magnetic field (Figure 2), the plateaus of Hall conductance at integer multiples of the conductance quantum demonstrate that the spin-valley degeneracy of the Landau levels is fully lifted, an indication of high device quality [6]. For small magnetic fields, the Hall resistance divided by the magnetic field gives the linear Hall coefficient (Figure 3). On either side of the charge neutrality point (~ 3.7 V), the Hall coefficient reaches a maximum and then falls off inversely with the magnitude of the carrier density. Our first measurements already demonstrate a Hall coefficient competitive with that previously reported for graphene at room temperature and GaAs at cryogenic temperatures [7,8].

To adapt these devices into a geometry suitable for scanning magnetic imaging, we will soon add a deep-etched trench surrounding the sensitive area, essentially positioning the Hall cross at the corner of the chip. Figure 4 demonstrates the deep-etch feature added to a SQUID magnetometer, and the inset clarifies the alignment geometry. To achieve this structure, we pattern the chip using photolithography (5x stepper) and etch through the SiO_2 and Si layers (Oxford 100 and Plasma-Therm Versaline) to a total depth of ~ 12 μm. With the inclusion of this final step, the Hall probes will be ready to begin scanning over test samples to characterize the point spread function of the probe and to calibrate the conversion between Hall voltage and magnetic field.

References:

[1] M. E. Huber, et al., Rev. Sci. Inst. 79, 053704 (2008).

[2] J. R. Kirtley, et al., Rep. Prog. Phys. 73, 126501 (2010).

[3] L. Wang, et al., Science 342, 614 (2013).

[4] P. J. Zomer, et al., Appl. Phys. Lett. 105, 013101 (2014).

[5] M. Ben Shalom, et al., Nat. Phys. 12, 318 (2016).

[6] F. Amet, et al., Phys. Rev. Lett. 112, 196601 (2014).

[7] J. Dauber, et al., Appl. Phys. Lett. 105, 013101 (2014).

[8] K. Vervaeke, et al., Rev. Sci. Inst. 80, 074701 (2009).

Gigahertz Surface Acoustic Waves on Periodically Patterned Layered Nanostructures

CNF Project Number: 2369-15

Principal Investigator: Brian C. Daly[1]

User: Weili Cui[2]

Affiliations: 1. Associate Professor of Physics, Vassar College; 2. Professor of Engineering, SUNY Maritime College

Primary Source of Research Funding: National Science Foundation Award Division of Materials Research-1709521

Contact: brdaly@vassar.edu, weilicui@yahoo.com

Website: http://pages.vassar.edu/ultrafast/

Primary CNF Tools Used: E-beam lithography, CVD, thermal evaporation

Abstract:

We used the ultrafast pump-probe technique known as picosecond ultrasonics to generate and detect surface acoustic waves on nanoscale aluminum (Al) lines on SiO_2 on silicon (Si). In all cases we identified a Rayleigh-like surface acoustic wave with wavelength equal to the pitch of the lines and frequency in the range of 5 GHz - 24 GHz. In some samples, we detected additional, higher frequency surface acoustic waves or independent modes of the Al lines with frequencies close to 50 GHz.

Summary of Research:

In recent work we measured surface acoustic waves (SAWs) in a complicated structure consisting of titanium nitride (TiN) wires of nanometer scale cross-section grown on a multilayered stack of porous and non-porous oxides on an Si wafer [1]. These unique samples yielded pitch-dependent frequencies that in some cases compared favorably with Rayleigh-like or Sezawa-like surface waves [2,3], but in other cases corresponded to modes that radiated significant acoustic energy into the substrate. In this work we studied a simpler set of samples consisting of aluminum (Al) lines on thin silicon dioxide (SiO_2) on Si and we detect multiple SAWs that can be identified by comparison with coarse-grained molecular dynamics simulations. The number of modes detected was found to depend on the pitch of the patterned Al as well as on the wavelength and polarization of the probe light. We detected Rayleigh-like SAWs and Sezawa-like SAWs with wavelength equal to the pitch of the Al lines as well as SAWs with wavelength equal to one-half or one-third of the pitch.

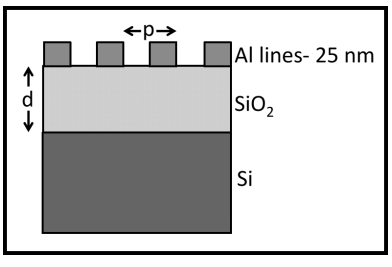

Figure 1: Schematic diagram of the samples. Film thickness d *was either 60 nm or 112 nm as measured by picosecond ultrasonics. Al lines pitch* p *varied from 1000 nm down to 140 nm. The duty cycle was close to 50% (+/- 10%) in all cases as measured by SEM.*

The ultrafast optical pump-probe experiment known as picosecond laser ultrasonics (PLU) has been described extensively in the literature [4]. We performed this experiment with a Ti:Sapphire oscillator operating at a 76 MHz repetition rate with pump wavelength of 800 nm and probe wavelengths of 800 nm or 400 nm. The ten patterned samples that we studied are illustrated schematically in Figure 1.

The samples were fabricated at the Cornell NanoScale Facility by the following process: thermal oxidation to produce the amorphous SiO_2 layer of thickness d = 60 or 112 nm, thermal evaporation of 25 nm of Al, and e-beam lithography and dry etching to create the nanometer scale Al pattern. The lines were etched perpendicular to the <110> direction in the Si substrate, they varied in pitch p ranging from 140 nm up to 1000 nm, and they were all etched near 50% (ranging from 40-60%) duty cycle. The patterned samples were placed into the optical setup, where pump and probe beams were both focused onto the same 20 μm diameter spot, so that anywhere from 20 to 140 periods of the pattern were strongly illuminated. The ultrafast pump pulses were absorbed by the Al lines, and the resulting rapid thermal expansion launched ultrasonic waves both downward into the SiO_2 film and Si substrate, and laterally as SAWs in the direction perpendicular to the line pattern. The ultrasonic waves can be detected by the time-delayed probe pulses due to transient changes in the reflectivity ΔR that they cause. The sources of these transient changes include the

dependence of the optical constants of the Al on strain as well as the changes in reflectivity of the optical grating produced by the nanostructure as it responds to the acoustic oscillations.

In this work, we focus on the signals caused by laterally propagating ultrasound and not the signals caused by acoustic waves traveling normal to the sample surface.

Figure 2a shows an example of the ΔR signal with 800 nm probe as a function of probe delay time for two of the samples (p/d = 400 nm / 112 nm and 200 nm / 112 nm). The exponentially decaying thermal background and the initial jump at $t = 0$ have been subtracted off so that the dominant oscillations are easier to observe. Figure 2b shows the Fourier transform for these two data sets. For both samples, the data are dominated by oscillations at two frequencies. As is expected, the smaller pitch sample produces higher frequency oscillations. The frequencies of the observed oscillations are strongly dependent on the pitch of the samples, and so it is evident that they must represent SAWs, independent bar modes, or a wave propagating very near to the surface of the sample. Other data sets show as few as one or as many as seven detected surface modes, and in the following sections we identify the nature of many of these modes. After an analysis of the many detected SAW frequencies in this experiment we conclude that we detected Rayleigh-like and Sezawa-like modes with frequencies as high as 50 GHz, as well as a number of independent bar modes.

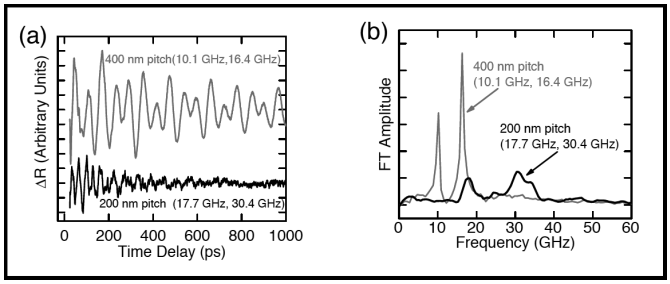

Figure 2: (a) ΔR for two samples with d *=112 nm and* p *= 400 nm and 200 nm. (b) Fourier transform amplitude of the signals in (a).*

We compared our results to analytical calculations of an SiO_2/Si structure and to coarse-grained molecular dynamics simulations of the complete structure in order to accurately label the detected modes.

References:

[1] M.M. Bjornsson, et. al., J. Appl. Phys. 117, 095305 (2015).

[2] B. A. Auld, Acoustic Fields and Waves in Solids (Krieger Publishing Company, Malabar, Florida, 1990), Vol. 2, Ch. 10.

[3] G. W. Farnell and E. L. Adler, in Physical Acoustics, edited by W. P. Mason and R. N. Thurston (Academic Press, New York, 1972), Vol. 9, p. 35.

[4] C. Thomsen, H. T. Grahn, H. J. Maris, and J. Tauc, Phys. Rev. B 34, 4129 (1986).

Magnetic Imaging of Ionic Liquid Gated Transition Metal Dichalcogenides

CNF Project Number: 2514-16

Principal Investigator: Katja Nowack

User: Alexander Jarjour

Affiliation: Laboratory of Atomic and Solid State Physics (LASSP), Cornell University

Primary Source of Research Funding: Cornell Center for Materials Research (NSF MRSEC, DMR-1719875)

Contact: kcn34@cornell.edu, abj46@cornell.edu

Primary CNF Tools Used: Heidelberg DWL2000, SC4500 evaporators, JEOL 6300, Veeco Icon AFM, Oxford 81

Abstract:

We report progress on developing superconducting ionic liquid-gated MoS_2 devices compatible with scanned probe microscopy. We have developed a spin-on ionic gate for our MoS_2 devices, allowing us to push the material into the metallic regime. We discuss progress on improving our nanofabrication to observe superconductivity.

Summary of Research:

Atomically thin exfoliated molybdenum disulfide (MoS_2) devices have been reported to superconduct at an *n*-type charge carrier density of ~ 10^{14} cm^{-2} [1] with a critical temperature of approximately ~ 2 K in a monolayer [2]. To achieve the high charge carrier density ionic gating has been employed in the literature, and we wish to replicate this approach while adapting it to be compatible with mesoscale imaging. Our group is interested in imaging the magnetic response of the superconducting state, using scanning Superconducting QUantum Interference Device (SQUID) microscopy.

This technique can be used to measure the superfluid density of a superconductor as a function of temperature, which can reveal information about the order parameter [3]. Recent work on superconducting MoS_2 indicates the order parameter may not be fully gapped, suggesting a non-Bardeen-Cooper-Schrieffer (BCS) superconducting state [4]. Superfluid density measurements would complement the existing data, further illuminating the nature of the order parameter of this system.

Our device fabrication is performed in the CNF. First, optical contact lithography is used to pattern liftoff resist for bond pads, long leads from the device area to the bond pads, and a large gate for biasing the ionic liquid. A completed device is shown in Figure 1 which includes these features. The SC4500 electron beam evaporator is then used to deposit a Ti/Pt/Au trilayer. The gold is wet etched in the gate region, exposing the platinum. Thus, the device side of the electrolytic capacitor is gold, and the gate side is platinum, with the aim of minimizing electrochemistry during gating. Using the polymer stamp transfer techniques developed for graphene heterostructures [5], MoS_2 flakes are transferred onto these prepatterned substrates, and any polymer residue is removed by a chloroform dip. Then, contacts are patterned to the flake using the JEOL 6300 electron-beam lithography system, connecting it to the long leads and bond pads. These contacts are then metalized in the SC4500 with Ti/Au.

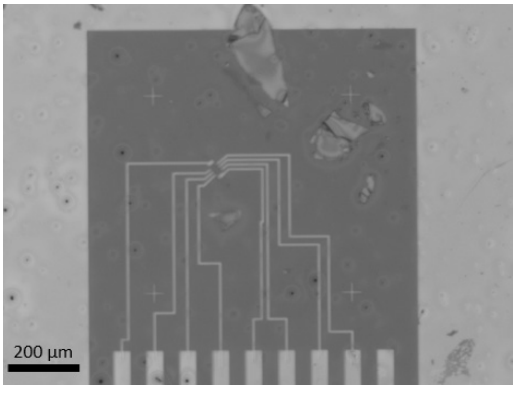

Figure 1: Spin-coated 380 nm ionic gel on MoS_2 few-layer device. Large surrounding metallic region is Pt gate, bars at bottom of image are optically patterned leads to bond pads.

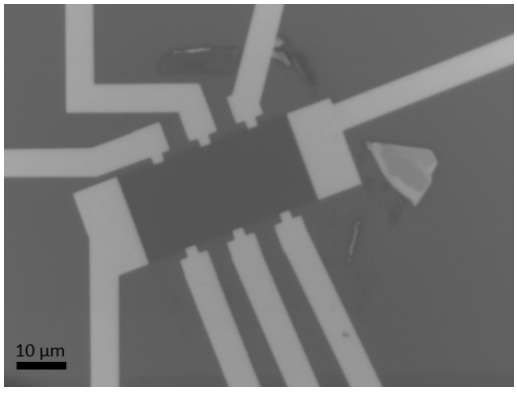

Figure 2: Few layer MoS_2 device fabricated by the authors.

Next, a Hall bar geometry is defined with the JEOL 6300, and the Oxford 80 is used to etch the MoS_2. Finally, a vacuum bake is used to remove any residue from the devices. A completed MoS_2 device before liquid gating is shown in Figure 2.

In our lab, an ionic gel is prepared from diethylmethyl(2-methoxyethyl)ammonium bis(trifluoromethylsulfonyl) imide (DEME-TFSI) and polystyrene-poly(methyl methacrylate)-polystyrene (PS-PMMA-PS). In an inert atmosphere, this gel is spun onto the devices, covering the MoS_2 flake and the platinum gate. The device is then transferred into a measurement cryostat insert with < 15 minutes of total air exposure, and pumped on for > 12 hrs at room temperature to remove water. The devices are then cooled to 4 Kelvin using a helium-4 cryostat, to determine if they are superconducting. An integrated variable temperature stage allows the sample temperature to be increased to the melting point of the ionic liquid (220 K) as it is insensitive to gate voltage changes below that temperature. We have not yet observed superconductivity in our devices, but are actively working on this issue.

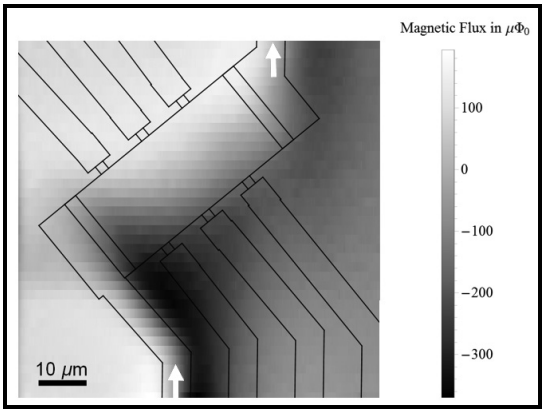

Figure 3: Scanning SQUID image of ionic liquid gated, metallic MoS_2 device. White arrows indicate current source and drain, black outline is device shape. Sample temperature approximately 10 Kelvin.

Magnetic imaging is performed in our 4 Kelvin cryogen-free scanning squid microscope. By spinning the gel to < 500 nm thick, we can image magnetism from currents flowing in the MoS_2 flake. Figure 3 shows such a magnetic image of one of our liquid-gated devices.

As we continue to improve our processing, we hope to soon observe superconductivity in these devices. We are working to ensure all our chemical processing is fully compatible with the MoS_2, as the superconductivity is expected to exist primarily in the first few atomic layers of the MoS_2 flake [1], which we suspect would make it sensitive to chemical processing during fabrication. We also suspect that the time in vacuum at ambient temperature may be insufficient to remove water absorbed from the air, and are working on developing a bake in the measurement cryostat to remove water from the gel.

References:

[1] J. T. Ye, et al., Science 338, 1193 (2012).

[2] D. Costanzo, et al., Nature Nanotechnology 11, 339 (2016).

[3] J.A. Bert, et al., PRB Vol 86 (2012).

[4] D. Costanzo, et al., Nature Nanotechnology 13, 483-488 (2018).

[5] P. J. Zomer, et al., Appl. Phys. Lett. 105, 013101 (2014).